Final Report for
Contract DE-FG07-99ID13763
Stanford Geothermal Program
September 2002

Table of Contents

1. STEAM-WATER RELATIVE PERMEABILITY IN FRACTURES

This project is being conducted by Research Assistant Chih-Ying Chen, Senior Research Engineer Kewen Li and Prof. Roland Horne. The goal of this research has been to gain better understanding of steam-water transport through fractured media and determine the behavior of relative permeability in fractures. According to the observation of Diomampo (2001), nitrogen-water flow through fractures is described most appropriately by using the porous medium (relative permeability) model. However, from the preliminary results in this research, steam-water flow in fractures shows a different behavior from nitrogen-water flow. The average steam-water relative permeabilities show less phase interference, and behave closer to the X-curve.

1.1 THEORETICAL BACKGROUND

Multiphase flow is an important mechanism in geothermal reservoirs, which are complex systems of porous and fractured media. Complete understanding of geothermal fluid flow requires knowledge of flow in both media. Normally, fractures are the main conduits for fluid. In geothermal reservoirs, the fluids, steam and water, are both derived from the same substance but in different phases. The phase change during steam-water flow is a physical phenomenon that does not occur in the multiphase flow of distinct fluids such as air and water, hence the multiphase flow properties are likely to differ. At present, the governing flow mechanism for boiling multiphase flow in fractures is still undetermined. There are two approaches commonly used to model multiphase flow in fractures, the porous medium approach and the equivalent homogeneous single-phase approach.

The porous medium approach treats fractures as connected two-dimensional porous media. In this model, a pore space occupied by one phase is not available for flow for the other phase. A phase can move from one position to another only upon establishing a continuous flow path for itself. As in porous media, the competition for pore occupancy is described by relative permeability and governed by Darcy's law. Darcy's law for single-phase liquid system is:

$$u_l = \frac{k_{abs}(p_i - p_o)}{\mu_l L} \tag{1.1}$$

where subscript l stands for the liquid phase, i for inlet and o for outlet; μ, p, L, u, k_{abs} are the viscosity, pressure, fracture length, Darcy flow velocity and absolute permeability respectively. The Darcy flow velocity is equal to

$$u = \frac{q}{bw} \tag{1.2}$$

with q as the volumetric flow rate, b the fracture aperture and w as the fracture width. Absolute permeability of a smooth-walled fracture is a function only of the fracture aperture (Witherspoon et al., 1980) as described in the relationship:

$$k_{abs} = \frac{b^2}{12} \tag{1.3}$$

For liquid phase in two-phase flow, Eq. 1.1 becomes

$$u_l = \frac{k_{abs}k_{rl}(p_i - p_o)}{\mu_l L}$$

(1.4)

where k_{rl} is the relative permeability of the liquid phase.

Similarly, Darcy's law derived for single-phase isothermal gas flow in porous media (Scheidegger, 1974) is:

$$u_g = \frac{k_{abs}(p_i^2 - p_o^2)}{2\mu_g L p_o}$$

(1.5)

with the subscript g pertaining to the gas phase.

In two-phase flow, Eq. 1.5 becomes

$$u_g = \frac{k_{abs}k_{rg}(p_i^2 - p_o^2)}{2\mu_g L p_o}$$

(1.6)

with k_{rg} as the gas relative permeability. The sum of the k_{rl} and k_{rg} indicates the extent of phase interference. A sum of relative permeabilities equal to one means the absence of phase interference. Physically this implies each phase flows in its own path without impeding the flow of the other. The lower is the sum of the relative permeabilities below 1, the greater is the phase interference.

Relative permeability functions are usually taken to be dependent on phase saturation. The two most commonly used expressions for relative permeability for homogeneous porous media are the X-curve and Corey curve (Corey, 1954). The X-curve defines relative permeability as a linear function of saturation:

$$k_{rl} = S_l$$

(1.7)

$$k_{rg} = S_g$$

(1.8)

where S_l and S_g are the liquid and gas saturation respectively. The Corey curves relate relative permeability to the irreducible or residual liquid and gas saturation, S_{rl} and S_{rg} :

$$k_{rl} = S^{*4}$$

(1.9)

$$k_{rg} = (1 - S^*)^2 (1 - S^{*2})$$

(1.10)

$$S^* = (S_l - S_{rl})/(1 - S_{rl} - S_{rg})$$

(1.11)

The equivalent homogeneous single-phase approach treats flow through fractures as a limiting case of flow through pipes. In this model, phase velocities in the fracture are equal and capillary forces are negligible. A continuous flow path is not required for movement of each phase. A phase can be carried along by one phase as bubbles, slug or other complex structures. As in pipes, flow can be described by the concept of friction factors and using averaged properties (Fourar et al., 1993):

$$\frac{(p_i - p_o)}{L} = \frac{\Pi f \rho_m V_m^2}{2A}$$

(1.12)

2

where Π is the fracture perimeter, A is the cross sectional area to flow, ρ_m average density and V_m as average flow velocity. The average density is described by:

$$\rho_m = \frac{\rho_g q_g + \rho_l q_l}{q_g + q_l} \tag{1.13}$$

The average flow velocity is equal to:

$$V_m = \frac{q_g + q_l}{A} \tag{1.14}$$

The friction factor, f, is derived empirically as a function of the averaged Reynolds number calculated by:

$$N_{Re} = \frac{2bV_m\rho_m}{\mu_m} \tag{1.15}$$

with μ_m as average viscosity:

$$\mu_m = \frac{\mu_g q_g + \mu_l q_l}{q_g + q_l} \tag{1.16}$$

There are several expressions used to relate friction factor and Reynold's number. The commonly used one for flow through fracture is the generalized Blasius form (Lockhart and Martinelli, 1949):

$$f = \frac{C}{N_{Re}^n} \tag{1.17}$$

with C and n as constants derived from experimental data.

According to the results from Diomampo (2001), nitrogen-water flow through fractures is described more appropriately by using the porous medium (relative permeability) approach based on the observations of the multiphase flow behavior. However in the steam-water case, the applicability of the two models for multiphase flow through fractures is still undetermined. From the preliminary results in this research, the steam-water flow shows a different behavior from the nitrogen-water case reported by Diomampo (2001).

1.2 LITERATURE REVIEW

The fluids in geothermal reservoirs, steam and water, are both derived from the same substance. However, they form different phases. The phase change during steam-water multiphase flow has made it difficult to investigate steam-water relative permeability. Even in multiphase flow without boiling, only a few published data are available for two-phase flow in fractures. Most of the studies have been done for air-water systems or for water-oil systems.

Earliest is Romm's (1966) experiment with kerosene and water through an artificial parallel-plate fracture lined with strips of polyethylene or waxed paper. Romm found a linear relationship between permeability and saturation, $S_w = k_{rw}$, $S_{nw} = k_{rnw}$ such that $k_{rw} + k_{rnw} = 1$ which represents the X-curve behavior. Fourar et al. (1993) artificially roughened glass plates with beads and flowed an air-water mixture between them.

Fourar and Bories (1995) did similar experiments using smooth glass plates and clay bricks. Both studies observed flow structures like bubbles, annular and fingering bubbles comparable to flow in pipes and depicted flow in fractures to be better correlated using the equivalent homogeneous single-phase model. Pan et al. (1996) observed the identical flow structures in their experiments with an oil-water system. They observed that a discontinuous phase can flow as discrete units along with the other phase. Pan et al. (1996) also found their experimental pressure drop to be better predicted by a homogenous single-phase model. All of these experiments showed significant phase interference at intermediate saturations.

Pruess and Tsang (1990) conducted numerical simulation of flow through rough-walled fractures. They modeled fractures as two-dimensional porous media with apertures varying with position. Their study showed the sum of the relative permeabilities to be less than 1, the residual saturation of the nonwetting phase to be large and phase interference to be greatly dependent on the presence or absence of spatial correlation of aperture in the direction of flow. Persoff et al. (1991) did experiments on gas and water flow through rough-walled fractures using transparent casts of natural fractured rocks. The experiment showed strong phase interference similar to the flow in porous media. The relative permeability data of Persoff (1991) and Persoff and Pruess (1995) for flow through rough-walled fractures were compared in Horne et al. (2000) against commonly used relative permeability relations for porous media, the X-curve and Corey curve, as shown in Figure 1.1. Diomampo (2001) performed experiments of nitrogen and water flow through both smooth- and rough-walled artificial fractures, leading to results that are also included in Figure 1.1.
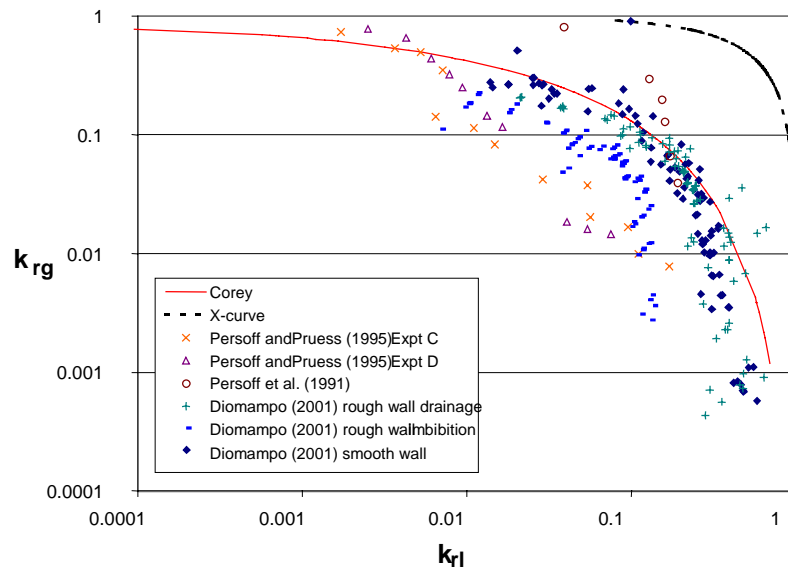

Figure 1.1: Compendium of previous measurements of air-water relative permeabilities in fractures (from Diomampo, 2001).

In the experiments of both Persoff (1991) and Persoff and Pruess (1995), flow of a phase was characterized by having a localized continuous flow path that is undergoing blocking

and unblocking by the other phase. Recent parallel plate experiments by Su et al. (1999) illustrate the same flow mechanism of intermittent localized fluid flow. Kneafsy and Pruess (1998) observed similar intermittent flow in their experiments with pentane through various parallel plate models made from glass, sandblasted glass or transparent fracture replicas. Diomampo (2001) also observed the intermittent phenomenon in her experiments. Furthermore, the results from Diomampo (2001) conform mostly to the Corey type of relative permeability curve (Figure 1.1). This suggests that flow through fractures can be analyzed by treating it as a limiting case of porous media flow and by using the relative permeability approach. These observations are contrary to the findings of Fourar et al (1993), Fourar and Bories (1995), and Pan et al. (1996).

Presently, the flow mechanism and the characteristic behavior of relative permeability in fractures are still not well determined. Issues such as whether a discontinuous phase can travel as discrete units carried along by another phase or will be trapped as residual saturation as in porous medium are unresolved. The question of phase interference i.e. whether the relative permeability curve against saturation is an X-curve, Corey or some other function, is still unanswered. The main objective of this study is to contribute to the resolution of these issues. Experiments on flow through smooth-walled and rough-walled fractures without boiling have been conducted by Diomampo (2001), who established a reliable methodology for flow characterization and relative permeability calculation for nitrogen-water flow. Currently, steam-water system experiments are in progress.

1.3 EXPERIMENTAL METHODOLOGY

The steam-water flow experiment is more complex than air-water experiment conducted previously by Diomampo (2001). The steam-water flow experiment has to be performed at high temperature, and there is a fundamental difficulty measuring how much of the fluid flows as steam and how much as liquid. The whole experiment system is illustrated in Figure 1.2, which shows the deaerated water supply, the fracture apparatus (inside the air bath), data acquisition system, and digital image recording (also see Figure 1.9).
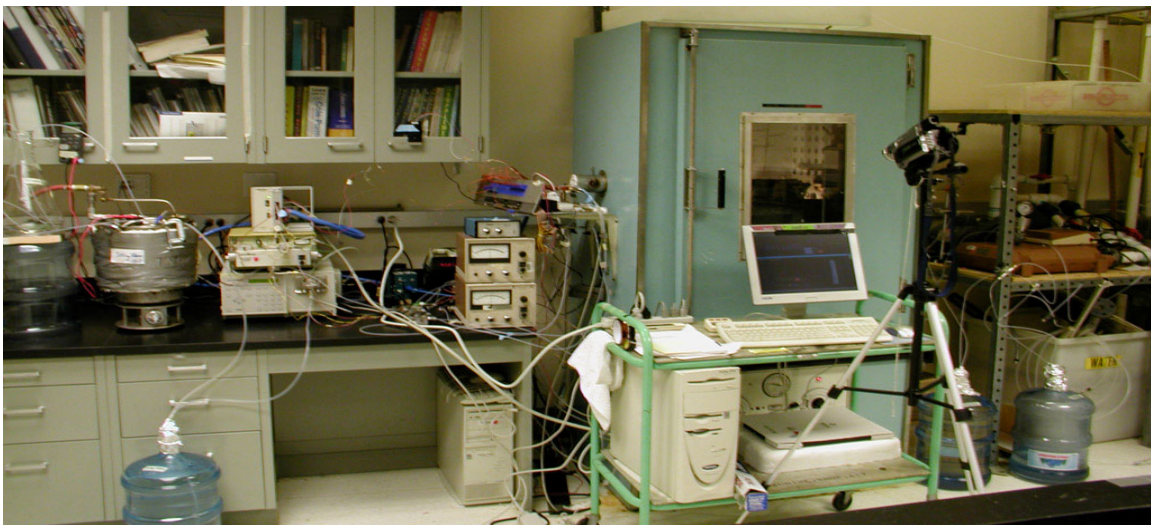

Figure 1.2: Picture of steam-water flow through fracture apparatus.

Fracture Apparatus Description

The fracture is created by a smooth glass plate on top of an aluminum plate, confined by a metal frame bolted to the bottom plate. The frame was designed to improve the seal and to prevent deformation of the glass due to system pressure. The metal frame has several windows and a mirror attached to it for flow visualization (see Figure 1.3 and Figure 1.4.)
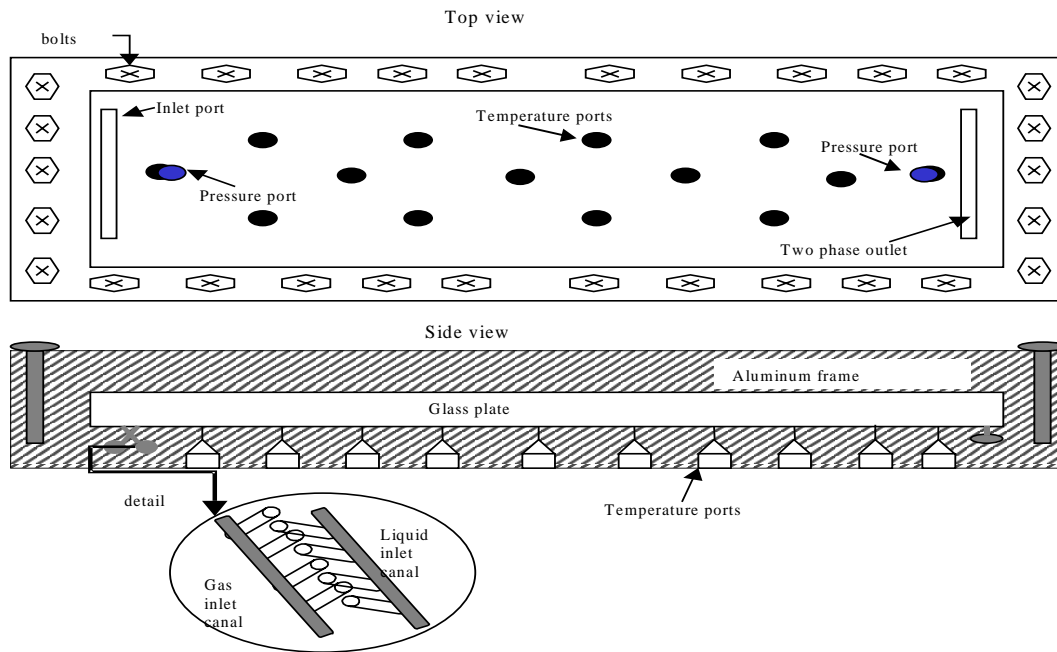

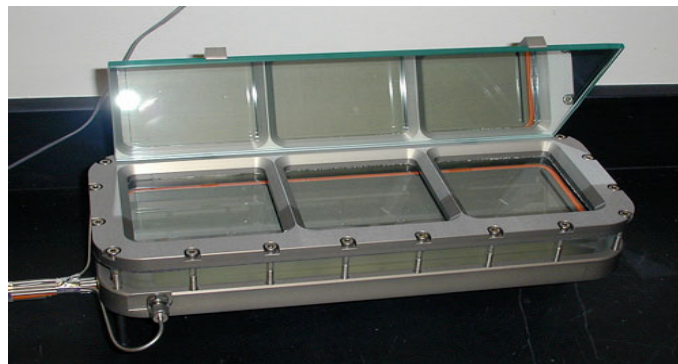*Figure 1.3: Schematic diagram of fracture apparatus.*

Figure 1.4: Picture of fracture apparatus.

An O-ring (Viton 1/8" thick #2-272) was placed in between the glass and aluminum plate as a seal (see orange color lining in Figure 1.4). Placing this O-ring in the channel was not sufficient to provide a good seal because the channel was custom made in width and length. Thinly cut rubber sheets were placed at the outer boundary to push the O-ring to the sides of the aluminum plate. These provided an excellent seal when compressed with the glass and metal frame. Since the O-ring is cylindrical in shape and the aluminum plate is rectangular, there is a narrow channel in between the O-ring and the plate when

squeezed together. A thin lining of copper-based adhesive (Permatex Ultra Copper) was applied to fill this channel. It is important to eliminate this channel for it serves as an easy conduit for the fluid to pass through instead of the fracture.

The phases enter the fracture through two separate canals. Each canal has several ports drilled in a way that they align on the surface (see Figure 1.3). In the nitrogen-water experiments both entry canals were used, but in the steam-water experiments only water was injected and the steam was created by boiling within the fracture itself. The surface of the fracture apparatus was designed such that there is an available 12 inch by 4 inch space for flow. Throughout this flow area, tiny temperature ports the size of needles were drilled. Needle-size ports were drilled so as to minimize surface discontinuity. A pressure port was drilled at each end of the flow path. The two-phase fluid exits through a single outlet. The apparatus was designed to be of sufficient length that end effects only influence a small part of the flow window − experimental observations have confirmed this to be true.

Fractional Flow Ratio Detector (FFRD)

One of the biggest challenges of the steam-water flow experiment is to measure the steam and water flow rates, since there is phase transition occurring when steam and water flow through the fracture. Therefore using flow meters to measure the rate of each phase becomes inappropriate, because it is always impossible to separate steam from water without any mass loss or gain. To overcome this situation, an in-situ fractional flow ratio detector (FFRD) was designed and constructed as shown in Figure 1.5. The principal of the FFRD is that different phases will have different refractive indices. A phototransistor (NTE 3038, NPN-Si, Visible, Vcbo 25V, Ic 20mA, Pd 50 mW, response time 1.5 μs) was installed inside the FFRD, producing different voltages when sensing different strengths of light. The water phase produces a higher voltage when flowing through the FFRD. In order to minimize the heat loss between the outlet of the fracture apparatus and the FFRD, the FFRD device was installed as close to the outlet of the fracture as possible (about 5cm distance). An example of the FFRD response signal during testing is shown in Figure 1.6.
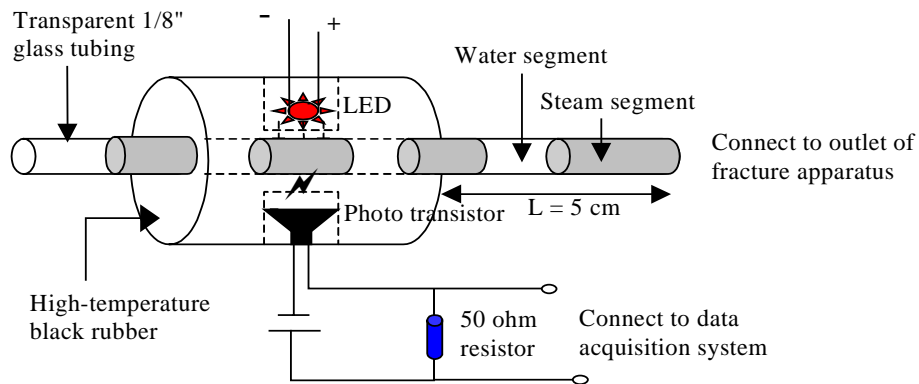

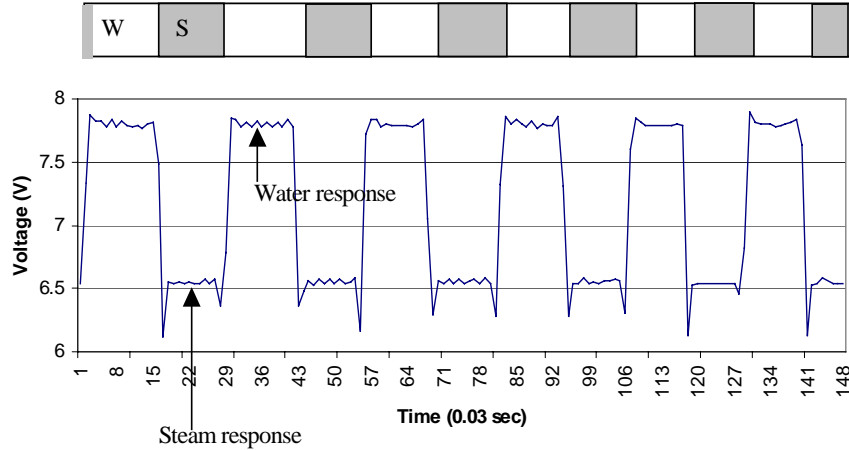*Figure 1.5: Schematic of fractional flow ratio detector (FFRD).*

Figure 1.6: The signal of steam and water detected from fractional flow ratio detector.

Once the steam and water responses are obtained from the FFRD, the statistical histogram is plotted and the steam and water phase flow ratios are obtained by determining the threshold of the histogram. This is shown in Figure 1.7 and Table 1.1.

The calibration test of FFRD has been completed as shown in Figure 1.8. As can be seen from Figure 1.8, at both high and low water flow rates the FFRD shows high accuracy in measuring fractional flow at different nitrogen flow rates. Even when the nitrogen flow rate is much higher than the water flow rate, the FFRD can recognize the fractional flow ratio over a period of several seconds. Therefore, the FFRD technology should be appropriate to calculate steam and water outlet flow rates.

Table 1.1: The analysis results of steam and water fractional flow ratios from Figure 1.7.

Bin	Frequency	Discrimination
6.2	287	Steam
6.4	603	Steam
6.6	7021	Steam
6.8	600	Steam
7	110	Steam
7.2	20	Threshold
7.4	146	Water
7.6	400	Water
7.8	3810	Water
8	3462	Water
More	0	

Steam Total	8631
Water Total	7828
Grand total	16459

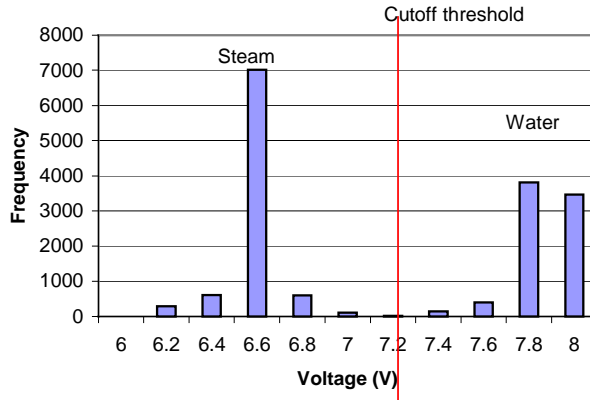| Fractional flow	
Steam	0.5243939
Water	0.4756061

8

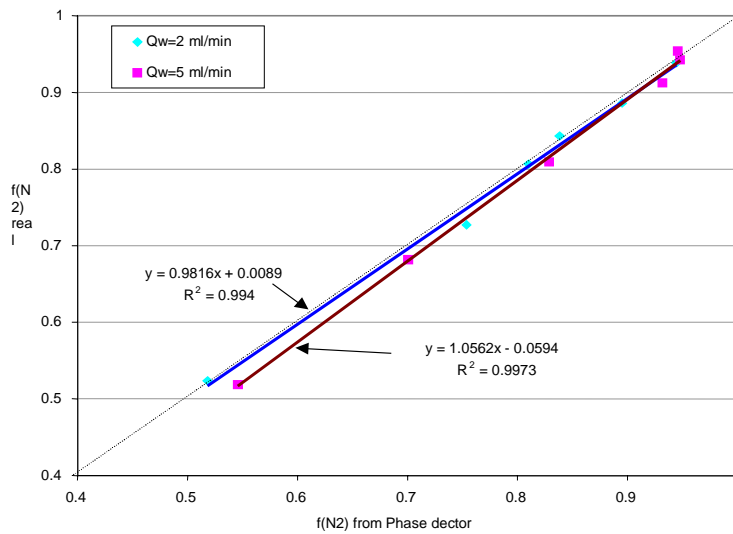*Figure 1.7: The histogram obtained from Figure 1.6.*

Figure 1.8: The calibration of FFRD in nitrogen-water flow.

1.4 CONTROL AND MEASUREMENT TECHNIQUES

There are two methods available to produce steam-water flow inside the fracture. One method is by injecting steam and water separately into the apparatus. The steam would be produced using a steam generator inside the air bath to boil steam from deaerated water. The other method is by injecting only deaerated water into the apparatus, after which the steam phase is produced by adjusting either pressure or temperature in the fracture. Since the steam quality from the steam generator is hard to control, the heat loss from the steam generator to the fracture apparatus is hard to determine, and there is a significant phase transformation at the moment when the injected steam and water meet in the inlet port, the latter method was used in this experiment.

The two factors that control the steam production are temperature and pressure. According to experience, adjusting pressure requires less equilibration time than adjusting temperature. To facilitate pressure adjustment, a physical back-pressure device

was connected to the outlet of the apparatus to constrain the pressure inside the fracture to a specific value. For water, a meter pump (Dynamax, SD-200) controlled the rate of injection. The water used in the experiment needs to be deaerated almost completely. To reach this quality, distilled water was evacuated using a vacuum pump for 2 hours, and then the water was boiled to achieve a low dissolved-gas condition. This distilled, deaerated water was used as the injection fluid. Figure 1.9 shows a schematic diagram of this configuration.
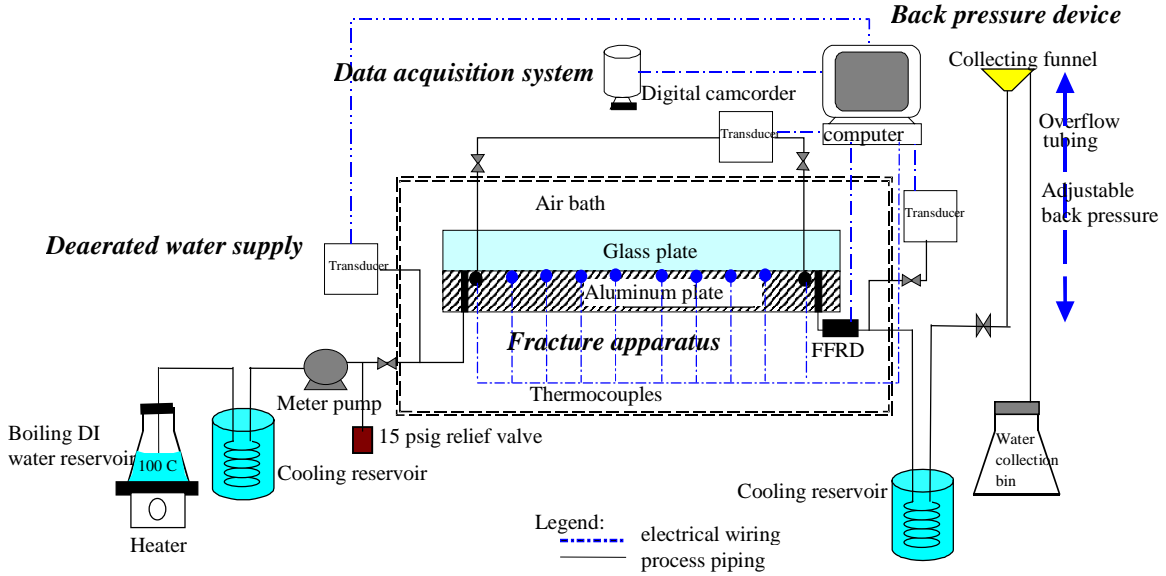

Figure 1.9: Process flow diagram for steam-water experiment.

Pressure

Low-range differential transducers were used to measure the pressure drop through the fracture, as well as the water inlet pressure and the two-phase outlet pressure. The liquid differential transducer (Celesco Transducer Model CD 10D range 0-5psi) was attached to both pressure ports inside the fracture to measure the pressure drop through the fracture. Another transducer (Celesco Transducer Model CD 10D range 0-25psi) was attached to the water inlet. The third transducer (Celesco Transducer Model CD 10D range 0-25psi) was attached to the two-phase outlet of the fracture apparatus. These transducers send electrical signals to the SCXI-1000 data acquisition device, which was monitored using the LabView® programmable virtual instrument software.

Flow rates, q_w and q_s

For steam and water flow rates measurement, the fractional flow ratio detector (FFRD) was used to measure the outlet steam and water fractional flow ratio, f_s and f_w.

$$f_s = \frac{q_{out,s}}{q_{out,t}} \tag{1.18}$$

$$f_w = \frac{q_{out,w}}{q_{out,t}} \tag{1.19}$$

where $q_{out,s}$ is the output steam flow rate, $q_{out,w}$ is the output water flow rate, and $q_{out,t}$ is the output total flow rate. Once f_s and f_w are obtained, it is easy to evaluate $q_{out,s}$ and $q_{out,w}$ by using mass balance if a steady-state condition is reached. In order to catch the fast and unsteady steam and water segment in the outlet tubing, The FFRD was connected to the SCXI-1000 data acquisition device, which has 50Hz maximum sampling frequency.

Once fractional flows are known, the steam and water flow rate can be calculated according to the mass balance under the assumption of steady state. The mass balance equation is:

$$m_{in} = q_{in,t}\rho_{w,at104^o c} = m_{out} = m_{out,w} + m_{out,s} = q_{out,t}(f_w\rho_{w,at104^o c} + f_s\rho_{s,at104^o c}) \qquad (1.20)$$

where, m_{in}, m_{out} stand for the input and output mass, $q_{in,t}$ and $q_{out,t}$ stand for input and output volumetric flow rates, ρ is the density, and f_s and f_w are steam and water fractional flows.

If f_s and f_w are known from FFRD data, the total output flow rate, $q_{out,t}$, can be obtained from Eq. 1.20:

$$q_{out,t} = \frac{m_{in}}{f_w\rho_w + f_s\rho_s} \qquad (1.21)$$

The end-point steam and water flow rates are:

$$q_{out,w} = f_w q_{out,t} = f_w \frac{m_{in}}{f_w\rho_w + f_s\rho_s} \qquad (1.22)$$

$$q_{out,s} = f_s q_{out,t} = f_s \frac{m_{in}}{f_w\rho_w + f_s\rho_s} \qquad (1.23)$$

Since the flow rates obtained are end-point flow rates, they can represent true flow rates under steady-state conditions. If the flow is in an extremely unsteady state, some mixed phase response will occur in the FFRD, and the flow rates calculated will become incorrect. However, if the flow is in quasisteady state (i.e. the steam or water flow rate increases at a fairly slow rate), flow rates obtained by this method should approximate the real flow rates except for a short delay of the phase response.

Saturation

Still images were taken from the recorded video. The data gathered from the video were correlated with the Labview data through the time read from the LCD monitor. Figure 1.10 shows a typical video image taken from the experiments. From the still image shown in Figure 1.10, saturation was computed by measuring the area that each phase occupied. The photographs were processed in a Matlab® program. The program first cuts the photograph to display just the image of the flow area. Using this cut image, the program does quadratic discriminant analysis (QDA) to group the pixels of the picture into three groups: the water phase, steam phase and the frame. The grouping is based on color differences. Saturation is calculated as total pixels of the liquid group over the sum of the steam and liquid groups. Figure 1.11 is a comparison of the gray-scaled image produced by the QDA program and the original cut photograph from the digital camcorder. The accuracy of the program in calculating the saturation can be related to the similarity in

details of the gray scale image to the true image. From the figure, it can be said that the program has reasonable accuracy.

Figure 1.10: Sample video image taken for steam-water runs.
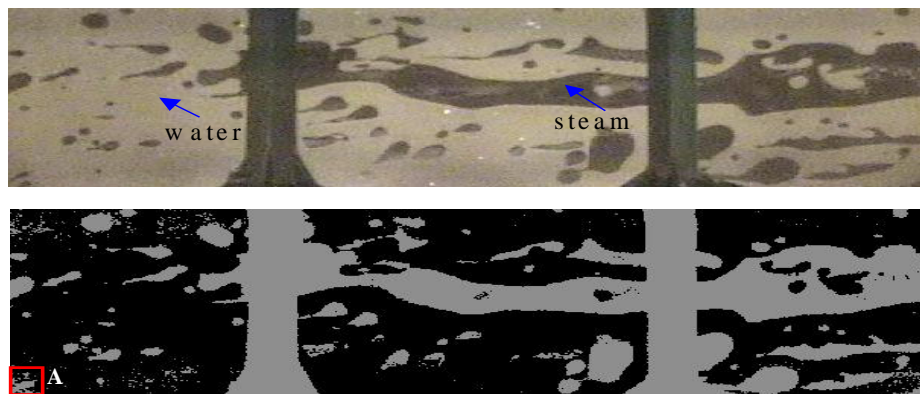

Figure 1.11: Comparison between the true color image of the fracture flow and gray scale image from Matlab QDA program used in measuring saturation.

Pan et al. (1996) also used this technique for measurement of saturation. This study noted that the sources of error in this technique were the quality of the photographs and the water film adsorbed on the surfaces of the plates with the latter being of minimal effect. Good quality photographs are the ones with clear distinction between the gas and liquid phase. Good lighting is necessary so that the colors in the image come out clearly. The lighting should also be positioned in a way that it does not produce shadow on the flow area. The program will mistakenly take the shadow as steam phase even if there is liquid (Zone A in Figure 1.11).

According to the nitrogen-water experiments by Diomampo (2001) and others, these fracture flow experiments are not expected to reach a perfect steady state. Instead, they are unsteady by nature. There are significant pressure fluctuations accompanied by saturation changes and the gas and liquid flow rates vary. Due to this behavior, the data acquisition task requires frequent gathering of instantaneous pressure, flow rate and saturation values. Instantaneous gathering of data was accomplished by the use of the digital video camcorder. Video shots were taken of the pressure, time and saturation data displayed all at the same time. Pressure and temperature data and related time were

displayed by the LCD monitor connected to the computer, which also ran the data acquisition system. The saturation was computed from the image of the whole flow area of the fracture. The methodology used to integrate all the data and signals and then calculate the steam-water relative permeabilities is illustrated in the flow chart in Figure 1.12.
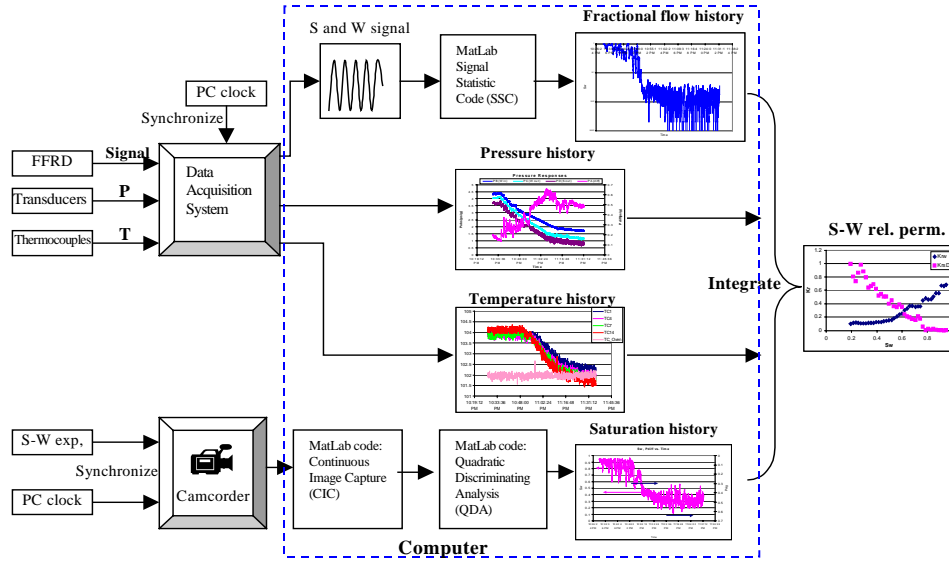

Figure 1.12: Data and signal processing flowchart.

1.5 PRELIMINARY RESULTS

Absolute Permeability of the Fracture

The absolute permeability of the fracture under water flow was measured at high temperature (~95°C) with different back pressures. High temperature makes the system close to the relative permeability experiment condition. Having different back pressures allows us to examine whether the back pressure is strong enough to alter the fracture aperture. If such an alteration happens, the subsequent experiments will be subject to the permeability correction according to their back pressure.

Figure 1.13 shows the absolute permeability of the fracture in deaerated deionized water flow under a 95 °C environment. According to Figure 1.13, the permeability is close to constant (~1020 darcy) except for one outlier at 1265 darcy when the back pressure is less then 4psig. An increasing permeability trend can be seen when the back pressure is greater than 4 psig, which means the top glass of the fracture may be lifted by high pressure or this may be due simply to measurement error. Fortunately, subsequent experiments will be just going to 4 psig maximum pressure. Therefore, the average permeability (1020 darcy) taken from 0 to 3 psig was adopted for the relative permeability calculation.
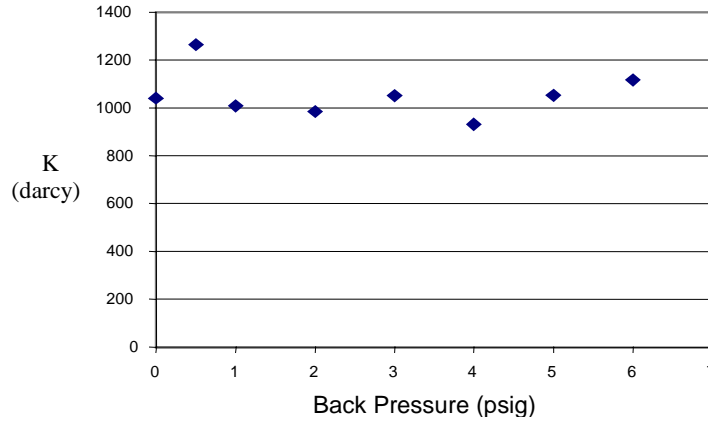
Figure 1.13: Absolute permeability in different back pressure at 95ºC

Steam- and Nitrogen-Water Flow Behaviors

A drainage steam-water flow through a smooth-walled fracture experiment has been conducted. The video images have been analyzed, and the corresponding saturation has been obtained satisfactorily. As observed from the video record, the steam-water flow behavior in the fracture is significantly different from the nitrogen-water flow behavior described by Diomampo (2001) in the same fracture.

Figure 1.14 shows four consecutive images (under high water saturation) taken when the water injection rate was 2 ml/min, temperature was 102ºC, and pressure was around 16.5 psia. The steam (dark part) never forms a stable path or channel, but behaves like moving fingers, slugs and bubbles. These physical phenomena are different from those observed in nitrogen-water flow by Diomampo (2001) as shown in Figure 1.15 which shows that nitrogen forms a nearly stable path.
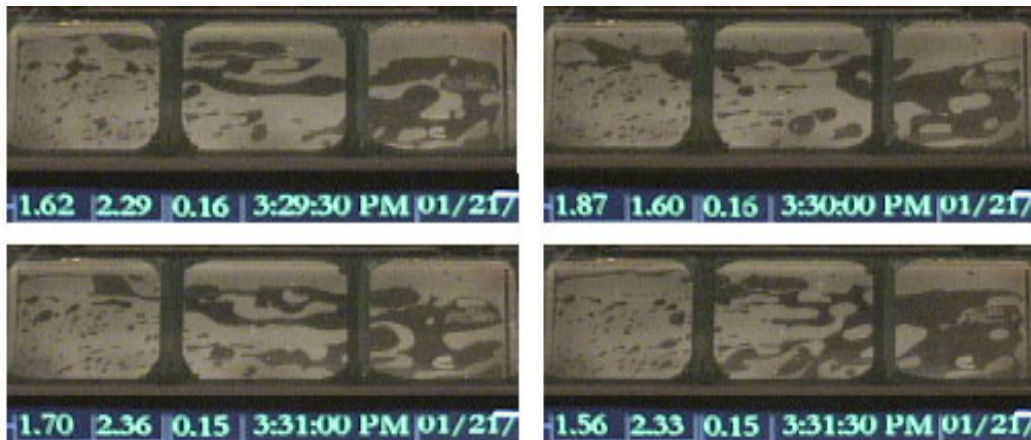

Figure 1.14: The continuous steam-water flow behavior in smooth-walled fracture under high water saturation (>65%) (steam phase is dark, water phase is light).
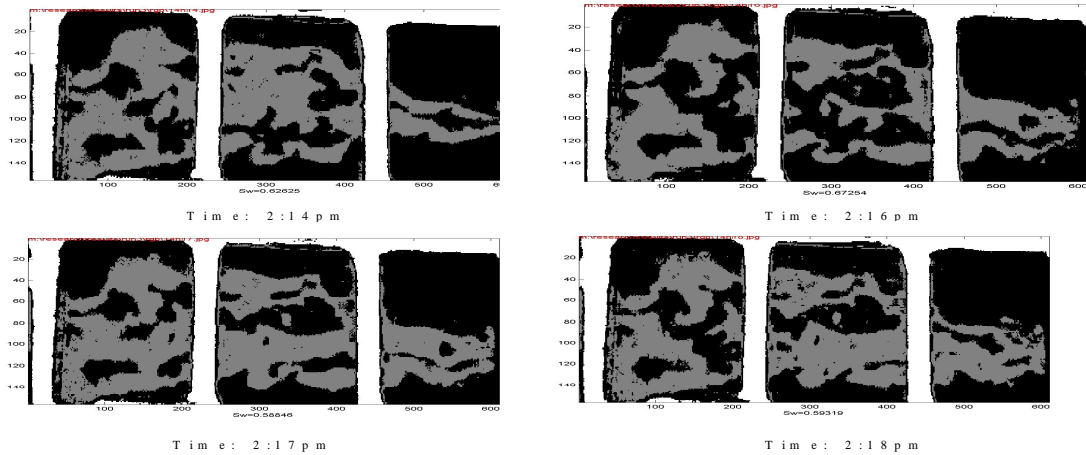
14

Figure 1.15: The continuous nitrogen-water flow behavior in smooth-walled fracture. Images showing the forming and breaking of gas flow path (light part) (images from Diomampo, 2001).

Comparing Figure 1.14 to Figure 1.15, there is less steam phase near the inlet (the left side) in the steam-water flow in comparison to the nitrogen phase near the inlet in nitrogen-water flow. This is because of the phase transformation from water to steam as pressure decreases in the steam-water flow. Hence the farther the water flows, the more steam it produces. This will be an important factor affecting the steam-water flow behavior under high water saturation situations (>65%). Figure 1.16 shows the steam-water flow under low water saturation (<15%). In this case, it is water that behaves like moving fingers, slugs (the white circle in Fig. 1.16) and bubbles. These physical phenomena are different from those observed by Diomampo (2001) in nitrogen-water flow. According to these preliminary findings, the steam-water flow in fractures might be more suitably described by the equivalent homogeneous single-phase approach.
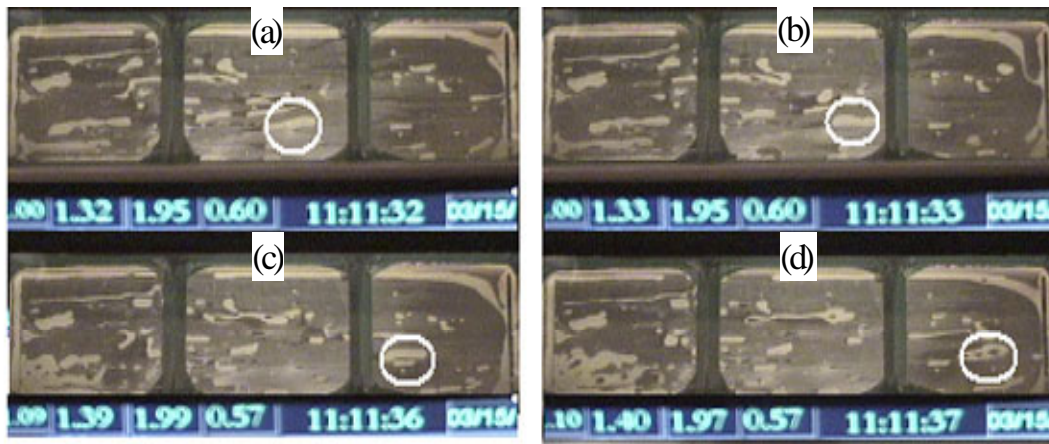

Figure 1.16: The continuous steam-water flow behavior in smooth-walled fracture under low water saturation (<15%). (steam phase is dark, water phase is light).

Unsteady Steam-Water Relative Permeability Experiment

An unsteady steam-water relative permeability experiment was conducted. In this experiment, the back pressure device in Figure 1.9 was modified to allow the pressure to decrease at a constant rate automatically. To accomplish this goal, a low RPM gearhead motor (2-6 RPM) and a pulley set was installed to control the back pressure. The detail of the back pressure device in the unsteady state experiment is shown in Figure 1.17.
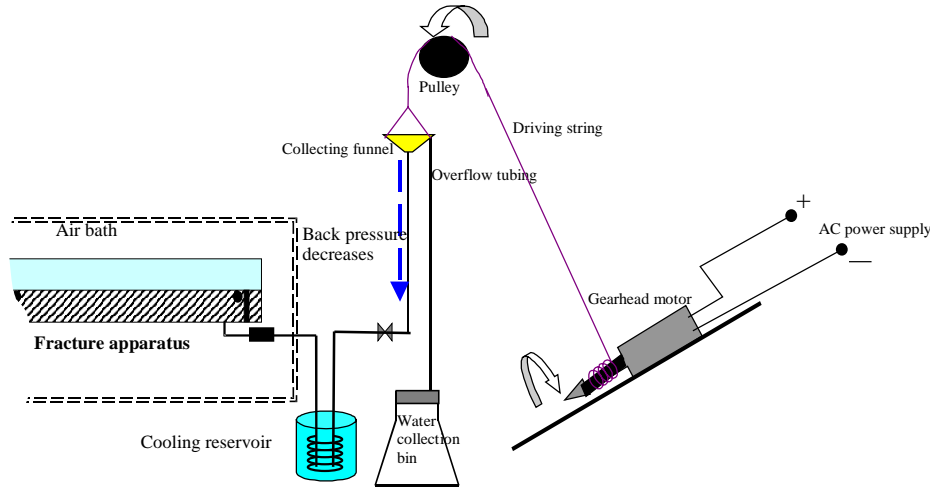

Figure 1.17: Schematic of back pressure control in unsteady state experiment.

The rotation rate of the gearhead motor was set to 3 RPM such that the rate of pressure decrease reaches 0.1psi/min. The starting back pressure was 3.3 psig. While the back pressure was decreasing continuously, the saturation images, pressure from each transducer, temperature from each thermocouple and fractional flow were recorded to the digital camcorder and to the computer via data acquisition system.

In the unsteady experiment, the back pressure was decreased continuously from 3.3 psig to 0 psig in 30 minutes. The experiment was recorded for this duration and for another 30 minutes after zero back pressure was reached, using the digital camcorder. This one-hour video was then captured and transformed to still JPEG images in one-second periods by the MatLab® CIC program. Therefore around 3600 images were obtained. These images were then subject to the Quadratic Discriminant Analysis (QDA) program to perform water saturation calculation. Figure 1.18 shows the input pressure (PB), output pressure (PC for water phase and PD for steam phase) and differential pressure (PA) responses during the experiment. The analysis result is shown in Figure 1.19. As can be seen in Figure 1.19(a), the change of the water saturation is consistent with that of pressure difference (inverted axis) along the fracture. Figure 1.19(b) also shows high correlation between the water saturation and pressure difference. This is consistent with the physical explanation. When the back pressure decreases at boiling temperature, the steam quality increases, which means steam saturation and volumetric flow rare increase. Since the volumetric increase of steam flow rate is much higher than the decrease of water flow rate according to mass balance, the pressure drop also increases. The saturation and pressure fluctuations in Figure 1.19(a) are due to the unsteady nature of the flow.
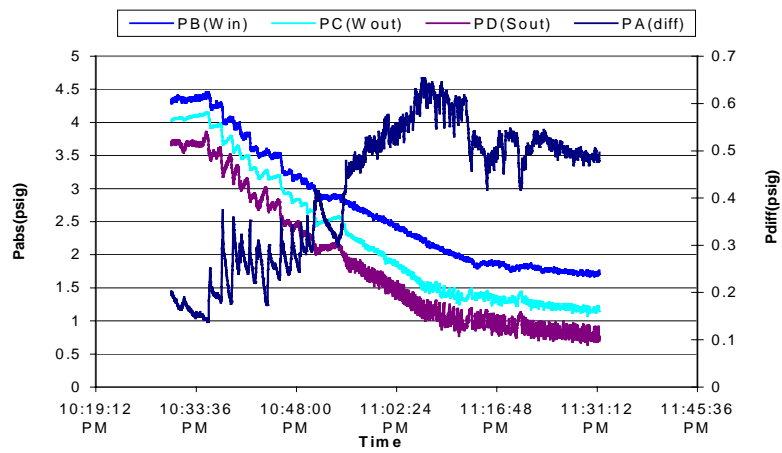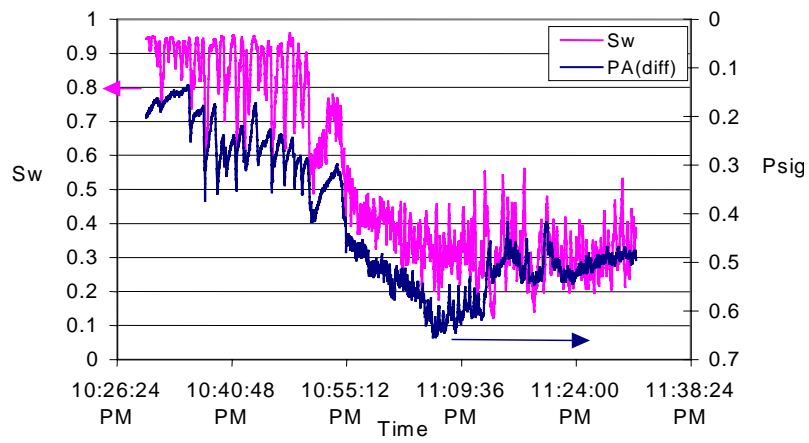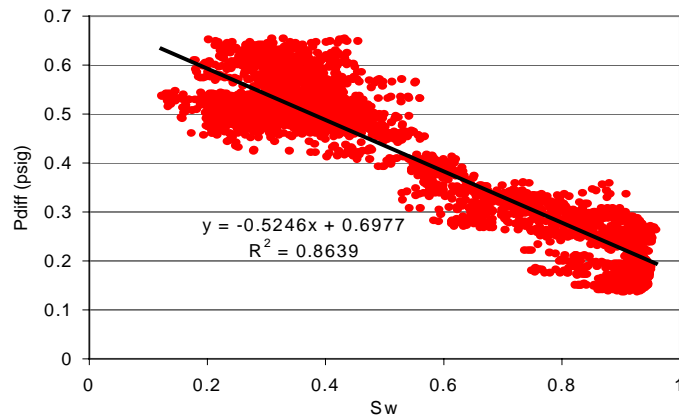
*Figure 1.18: Pressure responses during unsteady experiment.*

(a)

(b)

Figure 1.19: Water saturation versus pressure difference in unsteady experiment.

17

The signal of steam and water response from the FFRD was sent to the MatLab Signal Statistical Code (SSC) to perform the fractional flow calculation. Figure 1.20(a) presents the result of the water fractional flow response and saturation versus time. The y-axis of f_w is logarithmic whereas that of S_w is linear. Again, the trend of water fractional flow is consistent with that of water saturation. However, some offset of f_w and some mismatch of amplitudes in these two curves was found (Figure 1.20(b)). This may be due to both measurement error and computer analysis error. The offset of the f_w curve results mainly from the delay of the saturation response from the fracture to the FFRD at the outlet of the aparatus and the smoothing effect due to the discretized period, i.e. the period used to calculate one point of f_w. These errors would play an important role in the relative permeability calculation as will be shown later in this section.
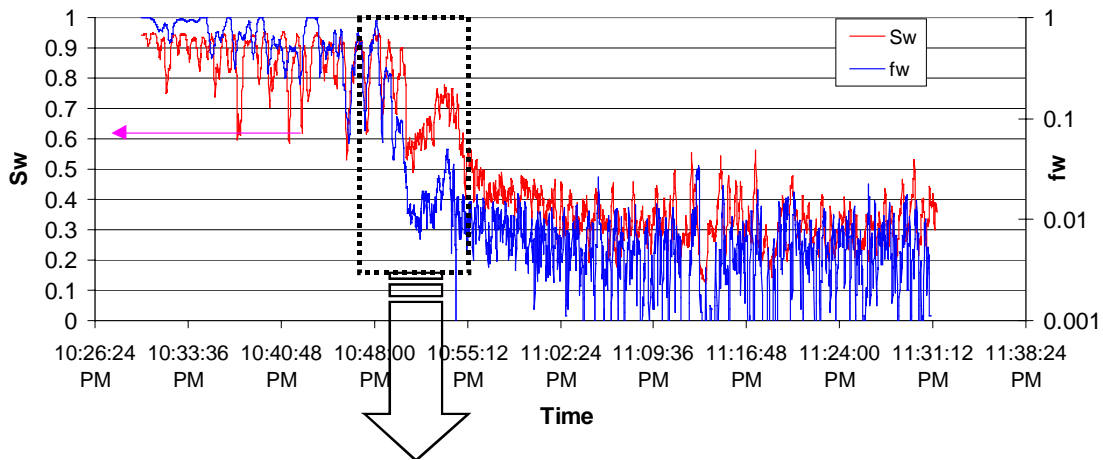
(a)
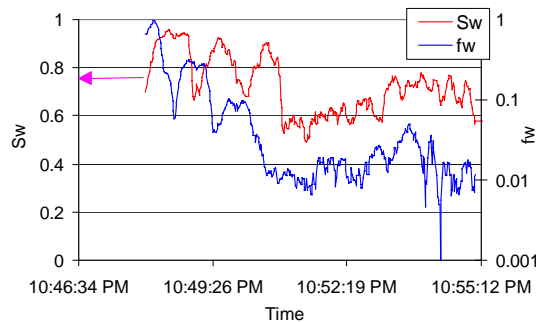
(b)

Figure 1.20: Water fractional flow (f_w) and saturation (S_w) versus time in the unsteady experiment.

The temperature distributions as functions of position and time are shown in Figure 1.21 and 1.22 respectively. From Figure 1.21, the temperature change from upstream to downstream in the fracture is within 0.5°C. However, a near 2°C temperature difference between the fracture and air bath in the initial single-phase (water) flow can be seen in Figure 1.22. This results from the warm-up effect caused by the lighting system installed at the back of the fracture apparatus. When steam quality increases, due to the high

18

velocity and lower conductivity of steam, the apparatus temperature will approach the environmental (air bath) temperature gradually as shown in Figure 1.22. This situation might affect the experimental result if the energy balance and heat loss calculations are applied, since the condition is not adiabatic. However, the effect may be limited if the steam and water flow rates are obtained from the FFRD directly.
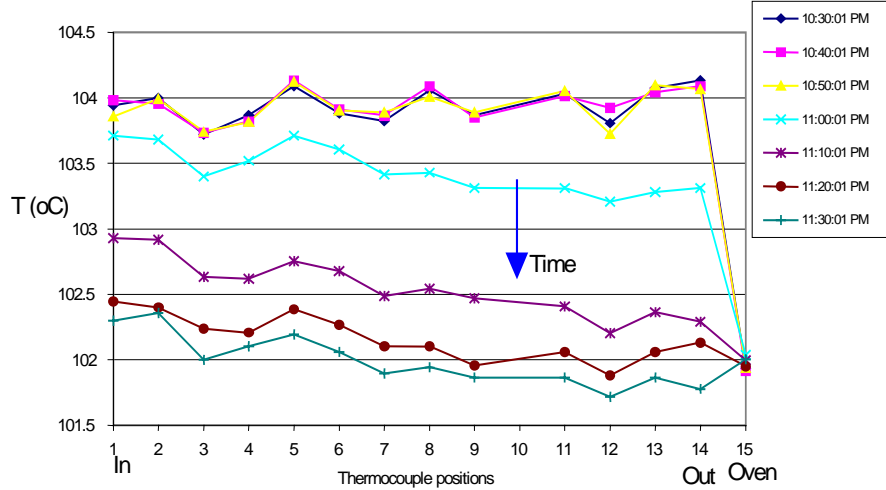

Figure 1.21: Temperature distribution through the fractures in steam-water unsteady experiment.
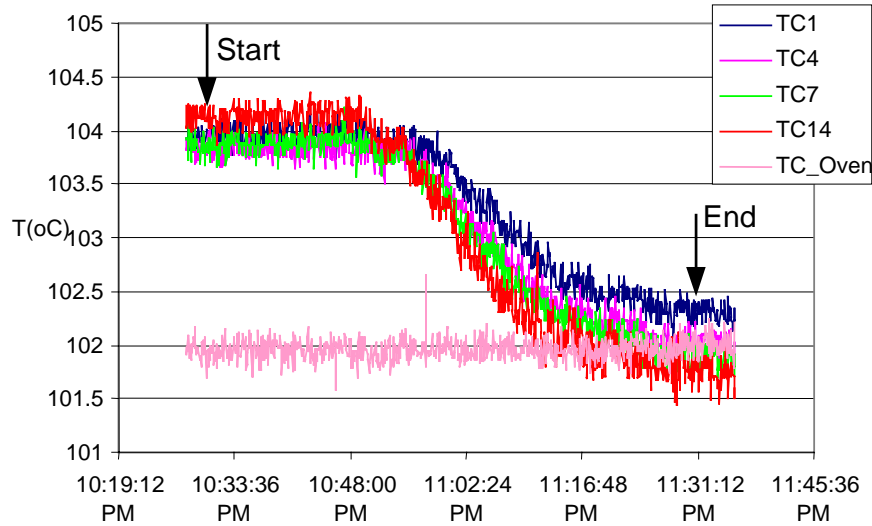
Figure 1.22: Temperature history in steam-water unsteady experiment.

After combining the pressure, temperature, saturation, fractional flow information in Figures 1.19, 1.20, and 1.21, the steam-water relative permeabilities can be calculated by using Eqs. 1.4, 1.6, 1.22 and 1.23. Figure 1.23 is the calculation result of 2670 data points out of a total of 3660 points. The remaining 990 points were either negative or unphysical (for example $k_r \gg 1$) due to measurement error or noise. The k_{rw} curve behaves smoothly, whereas the k_{rs} curve is very scattered. As mentioned before, this scattered effect may be partly associated with the measurement errors of both steam and water flow rates but seems to be caused more prominently by the fluctuating nature of the flow. The detail of

this error is due to the delay of f_s and f_w measurement from the FFRD and the measurement error caused by extremely high-speed steam flow which collapses the water component into many tiny water drops that are hard to detect in the FFRD. This will lower the measurement accuracy significantly.
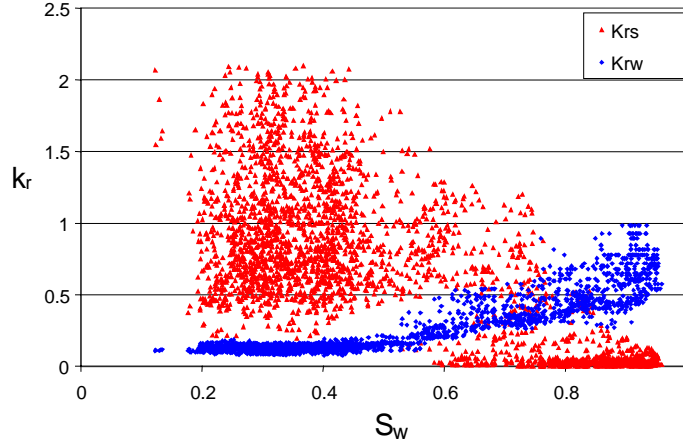

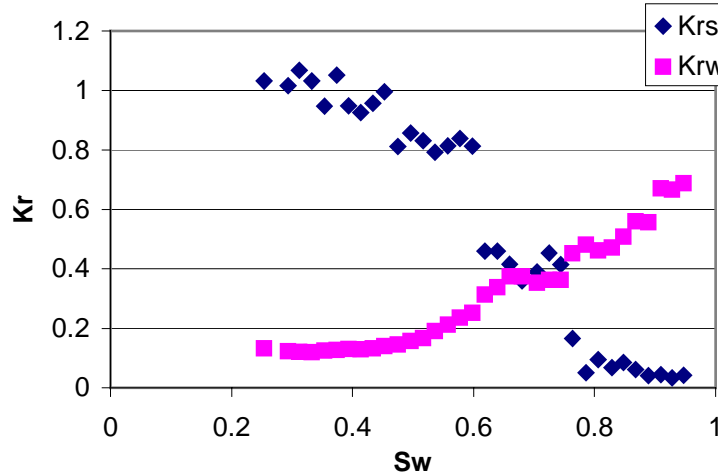*Figure 1.23: Steam-water relative permeability in the unsteady experiment.*

Figure 1.24: Steam-water relative permeabilities in the unsteady experiment by using 2% S_w averages.

Further processing was applied to Figure 1.23 to characterize the steam-water flow behavior. Figure 1.24 was obtained by averaging the relative permeability over 2% saturation ranges from Figure 1.23. The figure shows the fracture medium to be water wet since the two curves cross at near 70% water saturation. This is as expected because the aluminum and glass materials both have water-wet properties. What is interesting is that the sum of these two curves is close to 1 which indicates less phase interference. This result is different from the nitrogen-water relative permeabilities which showed a near Corey-type relative permeability behavior. Figure 1.25 shows the comparison of steam-water and nitrogen-water relative permeability curves. The nitrogen-water experiment was conducted by Diomampo (2001) who used the same fracture apparatus but at room temperature. The liquid curves have almost identical trends except in low

20

water saturation range where the steam-water case may lose some accuracy because of the error from the FFRD. On the other hand, the gas curves behave very differently. The steam curve shows a much more mobile character than the nitrogen curve, which can be seen from the higher relative permeability values in the steam curve. This phenomenon was also observed from the digital images.
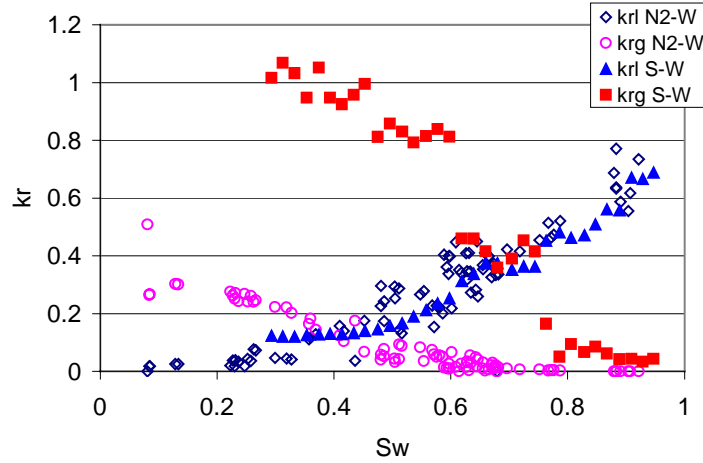
Figure 1.25: Comparison of relative permeability curves between steam- and nitrogen-water cases in the smooth wall fracture.

Figure 1.26 compares this result with previous research into air-water relative permeability in fractures. Most of these studies proposed that the air-water relative permeabilities in fractures follow Corey-type curves or below. However, as can be seen in Figure 1.26, the steam-water relative permeabilities behave closer to the X-curve.

Figure 1.26: Comparison of steam-water relative permeability with previous measurements of air-water relative permeabilities in fractures.

Application of Equivalent Homogeneous Single-phase Approach for Smooth-walled Fracture in Unsteady Experiment

Except using the porous medium model, the homogeneous single-phase pipe flow model was also applied to the data for the smooth-walled fracture in this unsteady experiment. The calculated friction factor with the modified Reynold's number in log-log plot is shown Figure 1.27. From the fitted linear equation, t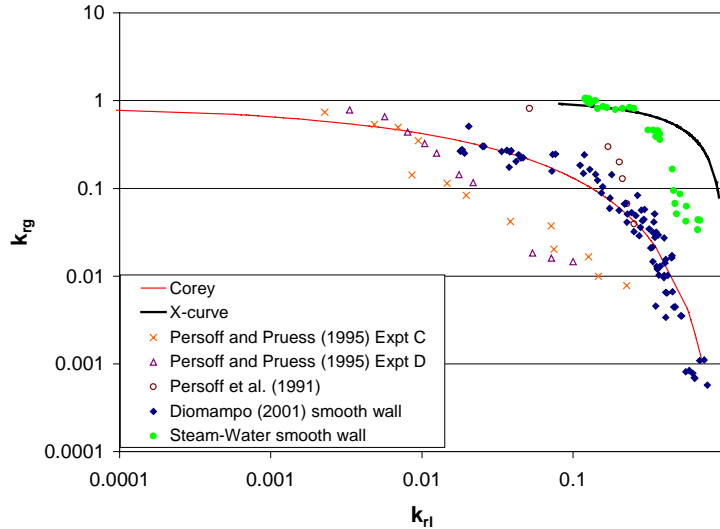he constants C and n in Eq. 1.17 are 18 and 1.1 respectively. Figure 1.28 compares this result to previous works for parallel plate experiments. The slope of the fitted line, -1.1, is close to the usual finding of negative unit slope for laminar flow. Also among all the studies, the data is closer to that of Fourar & Bories (1995).
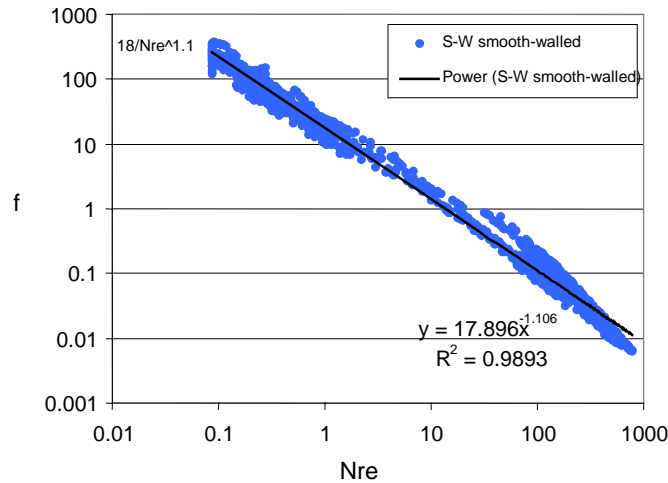

Figure 1.27: Logarithm of friction factor with logarithm of Reynold's number from data of the smooth-walled fracture in unsteady, steam-water experiment.
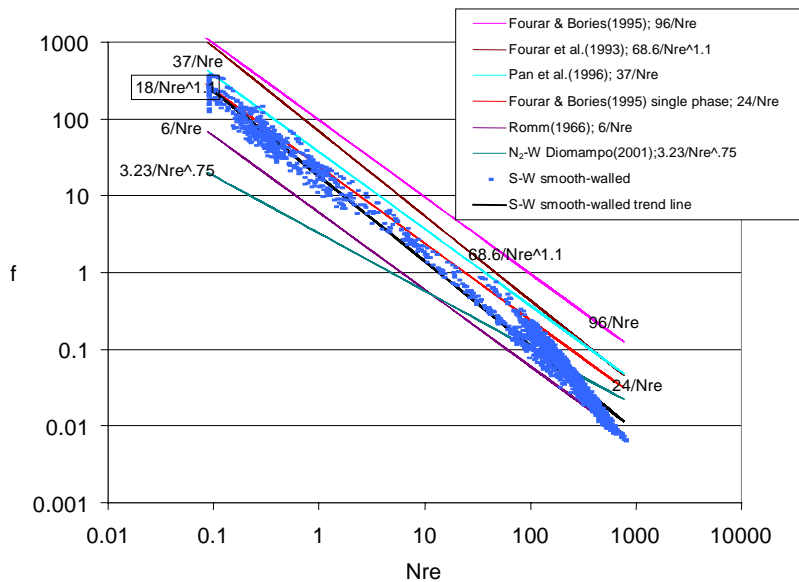

Figure 1.28: Friction Factor against modified Reynold's number for smooth-walled fracture in comparison to previous works.

From Figure 1.28, the *C* value (from Eq. 1.17) in the fitting curve of the unsteady, steam-water experiment is 18 which is close to the value of single phase (water) flow in smooth-walled fracture reported by Fourar & Bories (1995) (their value is 24). If only two-phase flow cases is considered, the *C* value in the unsteady, steam-water experiment is close that of Pan er al. (1996) (their value is 37), which was obtained from the oil-water flow in a smooth-walled fracture. The *n* value (from Eq. 1.17) in the fitting curve of the unsteady, steam-water experiment is 1.1 which is exact the same with the value of the air-water flow in a smooth-walled fracture presented by Fourar (1993) and close to all other researches which suggested the unity of *n* value. Overall the fit of friction factor as a function of Reynold's number with the steam-water experimental data shows consistency with previous researches except that done by Diomampo (2001).

AS mentioned in the section of theoretical background, the equivalent homogeneous single-phase approach treats flow through fractures as a limiting case of flow through pipes. As in pipes, the relationship of the pressure drop and friction factor can be described by Eq. 1.12. The pressure drop calculated from Eq. 1.12 in this unsteady, steam-water experiment was depicted in Figure 1.29. The data in Figure 1.29 again show scattered; however the trend line of it is very close to the 45° line. Similar to the way done in porous medium model, a 0.001psi range was taken for averaging the data in Figure 1.29. Figure 1.30 shows the averaged results which demonstrate good linearity and mostly follow the 45° line. However the scattered plot in Figure 1.29 shows the same phenomenon with the result obtained from the porous medium model in Figure 1.23. Therefore, the conclusion of which models represent steam-water flow best will not draw before steady, steam-water experiments are finished.
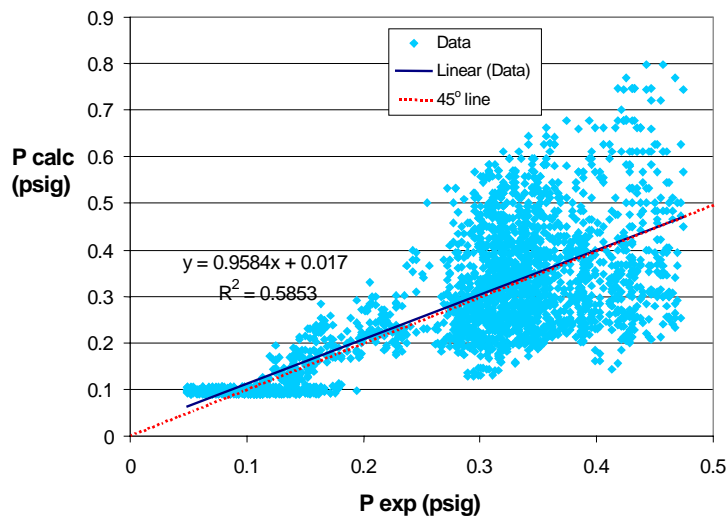

Figure 1.29: Comparison of the predicted pressure drop from homogeneous model and measured data for smooth-walled fracture in unsteady, steam-water experiment.
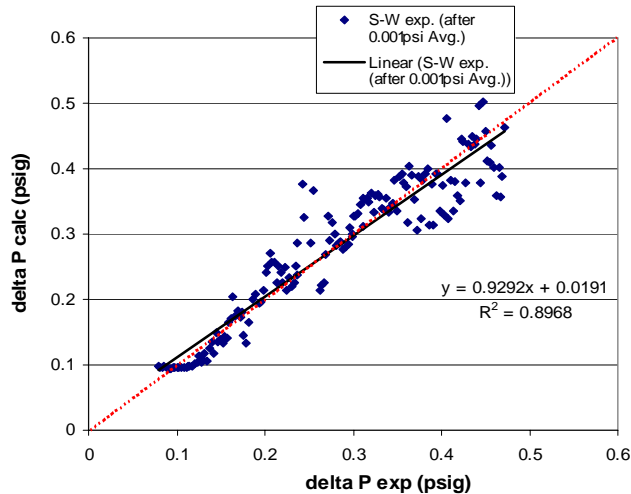
Figure 1.30: Calculated pressure drop from homogeneous model versus measured data for smooth-walled fracture in unsteady, steam-water experiment by using 0.001 psi averages.

1.6 DISCUSSION

The purpose in conducting the unsteady experiment first is that allows us not only to measure the relative permeability, but also to observe the transients of steam-water flow. Nevertheless, the unsteady experiments are also more uncertain. The steam phase relative permeability curve and the predicted pressure drop plot in homogeneous model in the unsteady experiment are scattered. This might be attributed to measurement error, or this may be the nature of steam-water flow in fractures. These results hamper us to suggest a better model to describe the steam-water flow by now. The sources of error may be attributed as follows:

End effect: As can be seen in Figure 1.16(c) and (d), there exist end effects near the inlet and outlet of the fracture. These will lead to overestimation of the water saturation. To overcome this problem, the very left and right parts of the image should be cut. Hence, the pressure measurement should be modified, either by drilling new pressure ports at inner positions or by using a method to infer the pressure from the saturation temperature.

Pressure oscillation: This resulted from boiling inside the pressure tubing. The boiling produces steam phase inside the pressure tubing in which only water phase is expected to exist. Unfortunately, this two-phase coexistence is unsteady. The evaporation and condensation rates depend highly on the system pressure and temperature.

Saturation calculation error: The quadratic discriminant analysis program will lose accuracy if there is some fog or cloudiness on the surface of the top glass of the fracture. This will overestimate the water saturation.

Flow rate measurement error: During steam-dominated flow, the liquid segments inside the FFRD will collapse and form small water. Further nitrogen-water corrections will be developed at extremely high air flow rate to address this problem.

24

Heat gain and loss: The illumination bulbs seem to heat the fracture apparatus. The temperature loss through the fracture is less than 0.5°C. These effects are still under investigation.

1.7 PRELIMINARY CONCLUSIONS

Based on the study, the following preliminary conclusions may be drawn:

1. The steam-water flow behavior in fractures is different from that of nitrogen-water flow. According to the observations of the steam-water flow video, the steam-water flow in fractures is closer to the homogeneous single-phase behavior.

2. When applying the porous medium approach to model steam-water flow in fractures, scattered steam-phase relative permeability values were obtained, which may be due either to the error of steam and water flow rate measurement and calculation or to the unsteady nature of steam-water flow.

3. The average steam-water relative permeabilities show less phase interference in comparison to the nitrogen-water cases reported by Diomampo (2001). Also, comparing with previous research into air-water relative permeabilities in fractures, the average steam-water relative permeabilities behave closer to the X-curve.

4. When applying the equivalent homogeneous single-phase approach to model steam-water flow in fractures, the modified Reynold's number and friction factor show good consistency with some previous researches. However, scattered results of the predicted pressure drop from homogeneous model versus measured pressure drop were obtained, which may be also due to the same reason as described above.

1.8 PREPARATION FOR FUTURE EXPERIMENTS

New experiments will need to focus on steady-state flow and on improving the accuracy of the measurements. Consistent and repeatable results should be obtained to confirm the steam-water flow behavior in fractures. In order to compare steam-water and nitrogen-water behavior, a nitrogen-water relative permeability experiment is scheduled under the same conditions as the steam-water experiment (high temperature, similar flow rates and identical analysis method). After that the steam-water relative permeability experiment will be conducted in rough-walled fractures. The detailed design and expected improvement of the steady experiment are described as follows:

Improvement of FFRD Accuracy

As mentioned earlier, the flow rate measurement may contribute one of the major errors in the relative permeability calculation. After reviewing the unsteady experiments done so far, we discovered that our FFRD was not sufficiently sensitive to capture the fractional flow of water, f_w, under high steam-water ratio conditions. According to the previous experiment and calculation, when steam phase relative permeability, k_{rs}, is 0.75, the water fractional flow, f_w, needed is only 0.01. By using the old FFRD and data acquisition system, the detected limit of f_w would only be around this magnitude, which means that when k_{rs} is more than 0.75, we may have a higher likelihood of obtaining inaccurate k_{rs} values due to the inaccuracy of the f_w measurements. This may be another factor that contributes to the scattered results in the plot of steam-water relative

permeabilities and the plot of predicted pressure drop against measured pressure drop (beyond the inherently unsteady nature of the flow).

Because of this realization, an improvement of the experimental system is in progress in both FFRD hardware and data acquisition parts. For the FFRD device (Figure 1.5), a thinner transparent glass tubing (3 mm OD, 1.65 mm ID) has been installed to replace the old tubing (3 mm OD, 1.4 mm ID). A new calibration was made. The result is shown in Figure 1.31. This replacement has improved the f_w detection limit of the FFRD from 0.01 to 0.005.
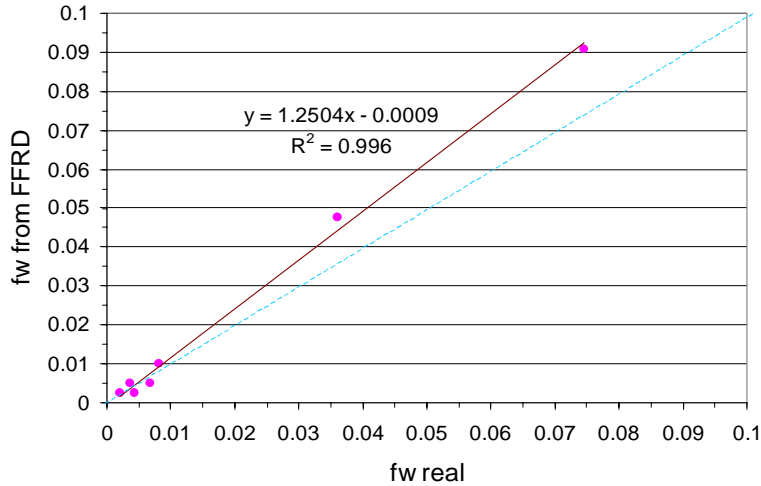
Figure 1.31: The new calibration of FFRD (Tubing ID=0.14mm, Q_w=0.5ml/min)

In order to capture fast (high frequency) steam-water flow in high steam-water ratio, a new, high-speed data acquisition board (NI PCI-6023E) was also installed. This replacement increased the data logging frequency from 50Hz to 250Hz. The new calibration incorporating in this high-speed data acquisition system is still under way. The desired f_w detected limit needed for future experiments is 0.001.

Modifications of Fracture Apparatus

Capillary end effect was another issue that influenced the previous unsteady experiment. In preparation for the planned steady experiments, some new pressure ports were drilled along the fracture for intermediate pressure difference measurement to minimize capillary end effect and facilitate intermediate absolute pressure measurement through the fracture. The complete measurement configurations through the fracture apparatus are shown in Figure 1.32(a) and (b).
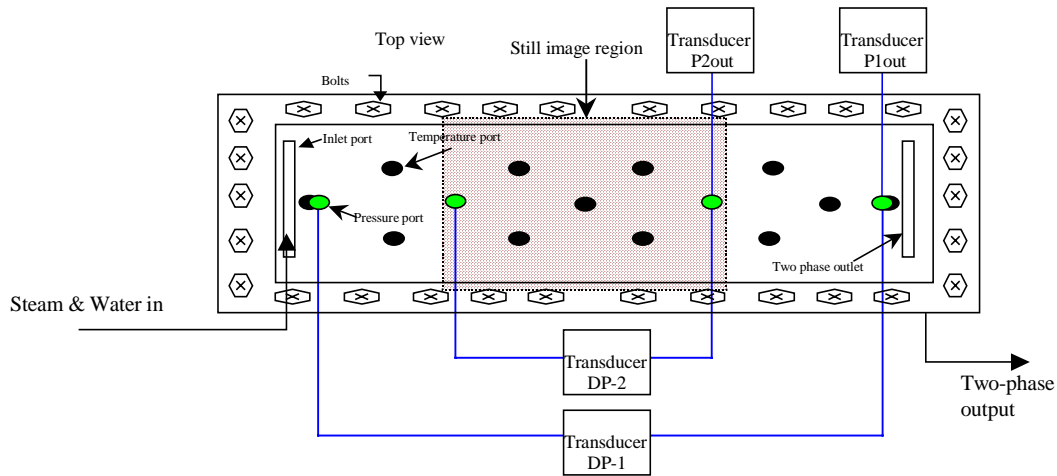
(a) Steam-water steady experiments.
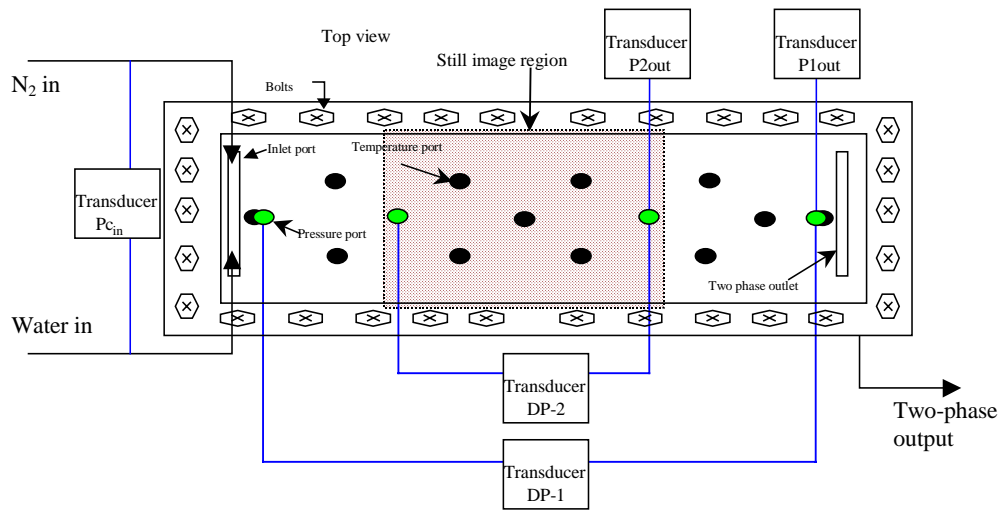
(b) Nitrogen-water steady experiments.

Figure 1.32: Schematic diagrams of pressure measurements in fracture apparatus in steady experiments. (a) Steam-water steady experiments. (b) Nitrogen-water steady experiments.

Still images will be taken both over the whole fracture region and in the intermediate region shown in Figure 1.32. Comparison of relative permeabilities obtained from these two flow regimes will be made to characterize the magnitude of the capillary end effect and flow stability.

Simulations of Experimental Data and Parameters

Simulations are necessary for predicting the range of future experimental data and some parameters, to make sure all data fall in the detectable ranges of the measuring devices. From previous unsteady experiments, a roughly X-type curve for steam-water relative permeabilities can be assumed as shown in Figures 1.33 and 1.34. The most important parameter that needs to be simulated in steam-water experiments is the minimum f_w in

large steam-water ratio situations. By using the X-curve shown in Figure 1.34 and the corresponding parameters shown in Table 1.2, the minimum f_w needed will be around 0.002. As mentioned previously, the detection limit of the current FFRD system is only 0.005, which means a more sensitive FFRD system or other flow rate measurement devices or methods need to be developed.
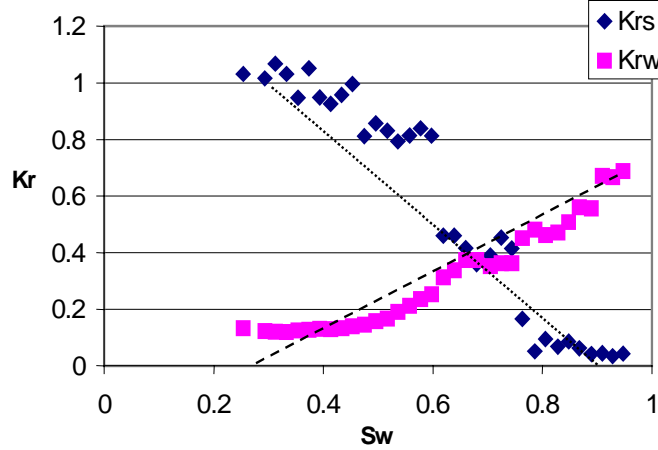
Figure 1.33: Experimental steam-water relative permeabilities from the unsteady experiment and their hypothetical, X-type curves (dash and dot lines).
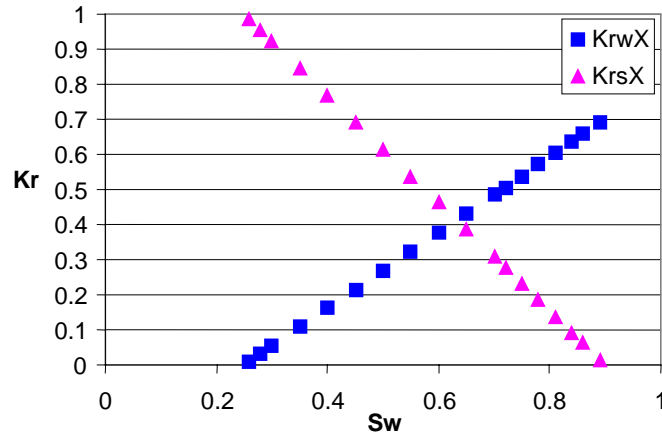
Figure 1.34: X-type curve used in water fractional flow prediction.

Table 1.2: X-curve parameters from Figure 1.34 and minimum f_w needed.

X-curve parameters				Minimum f_w need to detect
k_{rw0}	k_{rg0}	S_{wr}	S_{gr}	f_w min.
0.7	1	0.25	0.1	0.002

For the nitrogen-water simulation, since both fluid rates will be known, what is important are the ranges of nitrogen and water flow rates under some specific pressure drop. Rates should span a sufficient range to obtain more complete relative permeability curves. From nitrogen-water steady experiments done by Diomampo (2001), Corey-type curves

have been suggested to be representative of nitrogen-water relative permeabilities. Therefore, a traditional Corey-type curve shown in Figure 1.35 was used to predict the optimal data range of the nitrogen-water experiment. The simulation result of the nitrogen-water case is shown in Table 1.3. A metering pump with capacity of 0.1 ml/min ~ 200 ml/min and a gas mass flow controller with capacity of 2 ml/min ~ 2000 ml/min will be used in the experiments; therefore by setting the desired pressure drop and using Corey-type curves shown in Figure 1.35, the feasible fluid flow rates can be predicted.
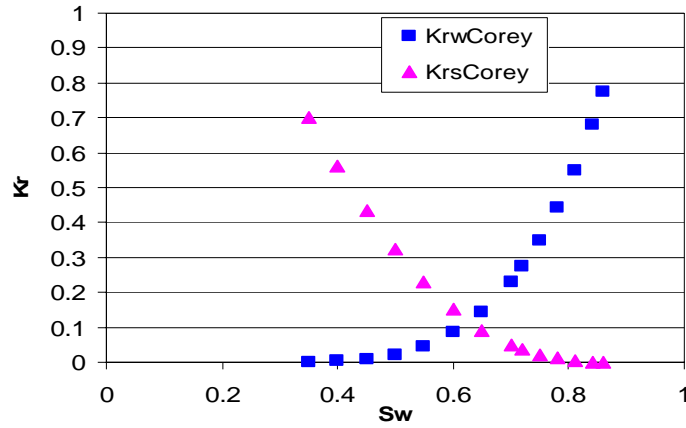
Figure 1.35: Corey-typr curve used in predicting nitrogen-water experimental data.

Table 1.3: Corey-type curve parameters from Figure 1.35 and data range predicted.

Corey-type curve parameters						Desired pressure drop	Water rate range		Nitrogen rate range	
n_w	n_g	k_{rw0}	k_{rg0}	S_{wr}	S_{gr}	Δp (psi)	Q_w max. (ml/min)	Q_w min. (ml/min)	Q_g max. (ml/min)	Q_g min. (ml/min)
4	2	1	1	0.25	0.1	0.4	186	0.1	2101	1.4

2. A CAPILLARY PRESSURE MODEL FOR GEOTHERMAL RESERVOIRS

This research project is being conducted by Senior Research Engineer Kewen Li and Professor Roland Horne. The objective of this project is to develop a capillary pressure model for geothermal reservoir engineering.

2.1 SUMMARY

Steam-water capillary pressure is often either ignored or determined artificially in geothermal reservoir engineering. However steam-water capillary pressure plays an important role in geothermal reservoir performance and may not be substituted by air-water capillary pressure. To this end, preliminary mathematical models have been developed to calculate drainage and imbibition steam-water capillary pressure respectively. Using these models, steam-water capillary pressure in geothermal reservoirs can be computed once porosity, permeability, and reservoir temperature are known. Experimental data of steam-water capillary pressure measured in Berea sandstone and inferred from adsorption tests in the rock from The Geysers were compared and used to develop the steam-water capillary pressure models in both drainage and imbibition cases.

2.2 INTRODUCTION

In recent years, much attention has been paid to the study of steam-water relative permeability (Sanchez and Schechter, 1990, Ambusso, 1996, Satik, 1998, Mahiya, 1999, Li and Horne, 1999, and Horne *et al*., 2000). However less attention has been paid to steam-water capillary pressure, even though capillary pressure is of equal significance to relative permeability and plays an important role in geothermal reservoir performance. As an example, Tsypkin and Calore (1999) investigated the vaporization process and found that capillary pressure can play a stabilizing role for the vaporization front. On the other hand, Li and Horne (2001a) showed that steam-water capillary pressure was significantly different from air-water capillary pressure.

Urmeneta *et al*. (1998) also studied the role of capillary forces in fractured geothermal reservoirs and found that capillary pressure tended to keep the vapor phase in the fractures and the liquid phase in the matrix. The numerical results from Urmeneta *et al*. (1998) showed that capillary forces control the transfer of fluids between fractures and matrix, the stability of the liquid-dominated two-phase zone, and the distribution of steam and water in geothermal reservoirs. Hence steam-water capillary pressure will influence the estimation of the energy reserves and production performance.

Sta. Maria and Pingol (1996) inferred values of capillary pressure from the adsorption data of Horne *et al*. (1995) for rock samples from The Geysers geothermal field. Persoff and Hulen (1996) inferred the vapor-water capillary pressure from adsorption data measured at room temperatures for The Geysers rock samples using different salt solutions to obtain a wide range of vapor pressures. Li and Horne (2001b) developed a method to calculate steam-water capillary pressure in Berea sandstone using the experimental data from steady-state steam-water flow tests conducted by Mahiya (1999).

The values of steam-water capillary pressure in both drainage and imbibition were obtained.

It would be useful for reservoir engineers to have an approach to estimate the values of steam-water capillary pressure for geothermal rocks with any porosity and permeability at any reservoir temperature. Until now, geothermal reservoir engineers have usually hypothesized the form of the steam-water capillary pressure curve used for numerical simulation, or ignored it entirely.

In this study, the steam-water capillary pressure data calculated by Li and Horne (2001b) in Berea sandstone were scaled and compared to the data from Persoff and Hulen (1996) using a *J*-function. Both drainage and imbibition steam-water capillary pressure models were developed based on these data for the application of geothermal reservoir engineering.

2.3 THEORY

Based on the Kelvin equation, Li and Horne (2001b) derived an equation to calculate steam-water capillary pressure from the experimental data of liquid phase pressure, temperature, and related parameters measured in a steady-state flow test. The equation is expressed as follows:

$$P_c = p_v - p_w = \frac{\rho_w RT}{M_w} \ln(\frac{p_0}{p_v}) \qquad (2.1)$$

where P_c is the capillary pressure. p_0 and p_v are the vapor pressures when the vapor-liquid interface is flat and curved respectively; R is the gas constant, T the absolute temperature, M_w the molecular weight of liquid, and ρ_w the density of liquid. The units used in Equation 2.1 are listed here. p_v, p_w, p_0: kPa (absolute), ρ_w: g/ml, R = 8310 (kPa.ml)/(°K.mole), T: °K, and M_w: g/mole.

In steady-state steam-water flow experiments (Mahiya, 1999), p_w and T can be measured at the same time and the same location, while p_0 can be calculated according to the measured saturation temperature. Therefore, p_v, as the only unknown parameter in Equation 2.1, can be obtained by Newton iteration. The capillary pressure is then computed.

Once the steam-water capillary pressure in the Berea sandstone was available, we could infer the steam-water capillary pressure in geothermal rocks. The procedure is described here. Capillary pressures in rocks with different porosity and permeability may be correlated using the *J*-function suggested by Leverett (1941) as follows:

$$P_c = \frac{\sigma \cos\theta}{\sqrt{\dfrac{k}{\phi}}} J(S_w) \tag{2.2}$$

where k, ϕ, S_w, and $J(S_w)$ are permeability, porosity, water saturation, and J-function respectively. Assuming that the J-function in both Berea and geothermal rock samples are the same, we can calculate the steam-water capillary pressure in geothermal rocks using the following equation:

$$P_c^G(S_w) = \frac{\sigma_G \cos\theta_G}{\sigma_B \cos\theta_B} \frac{\sqrt{\dfrac{k_B}{\phi_B}}}{\sqrt{\dfrac{k_G}{\phi_G}}} P_c^B(S_w) \tag{2.3}$$

Here $P_c^G(S_w)$ and $P_c^B(S_w)$ are the steam-water capillary pressures at a water saturation of S_w in a geothermal rock with a permeability of k_G and a porosity of ϕ_G and in a Berea sandstone with a permeability of k_B and a porosity of ϕ_B respectively. Considering that the temperatures may be different in the two systems, σ_B, the surface tension in the steam-water-Berea system, and σ_G, the surface tension in the steam-water-geothermal rock system, are introduced in Equation 2.3. Similarly, θ_G and θ_B are the contact angles in steam-water-Berea and steam-water-geothermal rock systems respectively. Equation 2.3 was derived by applying Equation 2.2 to each type of rock: Berea and geothermal. Since the contact angle in steam-water-geothermal rock systems is not available, we assumed in this study that the contact angles in both Berea and geothermal rock samples are the same. Furthermore, if we scale the experimental data to the same temperature, the surface tension will be the same. Therefore, Equation 2.3 would be reduced to:

$$P_c^G(S_w) = \frac{\sqrt{\dfrac{k_B}{\phi_B}}}{\sqrt{\dfrac{k_G}{\phi_G}}} P_c^B(S_w) \tag{2.4}$$

Based on Equation 2.4, the steam-water capillary pressure in geothermal rocks can be computed once the steam-water capillary pressure in the Berea sandstone, and the permeability and porosity in both Berea and geothermal rocks are known. We compared the steam-water capillary pressure calculated using Equation 2.4 for a rock from The Geysers geothermal field with the steam-water capillary pressure measured in the same rock by Persoff and Hulen (1996) using an adsorption method. Because the adsorption tests by Persoff and Hulen (1996) were conducted at a temperature of $28.5^{\circ}C$ and the steady-state flow tests were conducted at a temperature of $120^{\circ}C$, it is necessary to scale

up the capillary pressure measured by Persoff and Hulen (1996) to the same temperature, 120°C. This was achieved using the following equation:

$$P_c^{G,T_2}(S_w) = \frac{\sigma_{T_2}}{\sigma_{T_1}} P_c^{G,T_1}(S_w) \tag{2.5}$$

where $P_c^{G,T_1}(S_w)$ and $P_c^{G,T_2}(S_w)$ are the capillary pressure for the same rock at the same water saturation of S_w but at different temperatures of T_1 and T_2. σ_{T_1} and σ_{T_2} are the surface tensions at temperatures T_1 and T_2.

2.4 RESULTS

Steam-water capillary pressure in Berea sandstone. The drainage and imbibition steam-water capillary pressures measured by steady-state flow tests are shown in Figure 2.1 (Li and Horne, 2001b). The solid circles represent the drainage capillary pressure curve and the solid squares represent the imbibition capillary pressure curve. The curves represent the moving trend of the data points (the same for the rest figures except those specified).
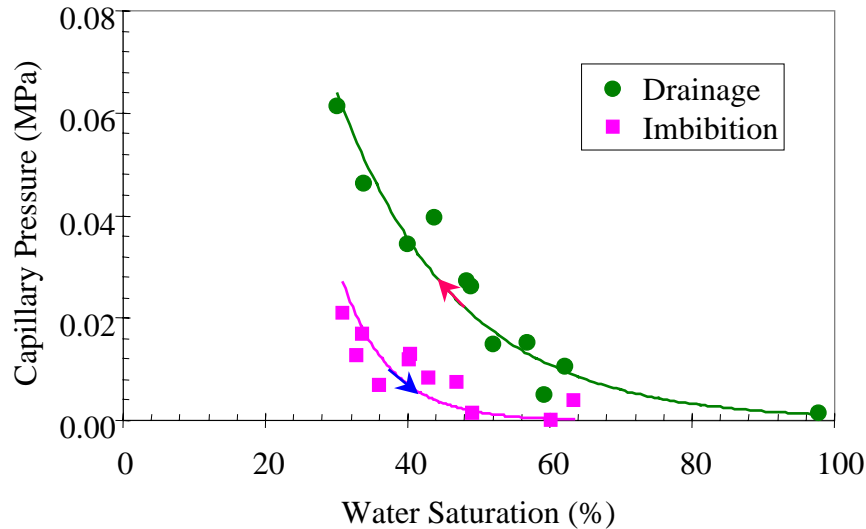

Figure 2.1: Steam-water capillary pressure curve (drainage and imbibition) calculated from the data of steady-state flow of steam and water in a Berea sandstone sample.

Steam-water capillary pressure in rock from The Geysers. As mentioned before, we can use Equation 2.4 to calculate the steam-water capillary pressure in geothermal rocks once the steam-water capillary pressure in a Berea sandstone sample is available. The purpose is to compare the results with those measured by Persoff and Hulen (1996) and hence evaluate the appropriateness of the assumptions of Equation 2.4. First of all, we need to know the porosity and permeability of the geothermal rocks. We based these

34

values on the core sample with a porosity of 1.9% and a permeability of 1.3 nd in which Persoff and Hulen (1996) measured the vapor-water capillary pressure at a temperature of 28.5°C. The steam-water capillary pressure data in both drainage and imbibition were computed using Equation 2.4 for this sample. Figure 2.2 shows the calculated capillary pressure curves. Note that the shape of the steam-water capillary pressure curves in Figure 2.2 is similar to that in Figure 2.1 but the values of steam-water capillary pressure are much greater because of the low permeability of The Geysers geothermal rock.
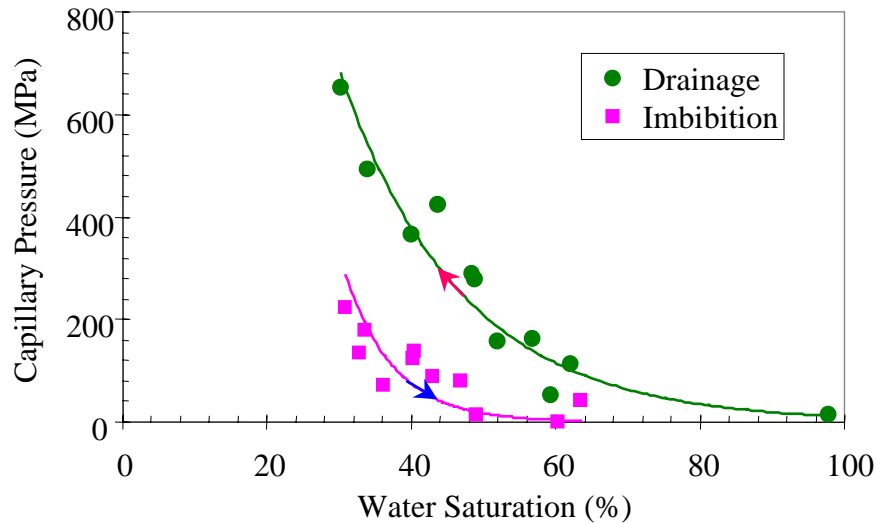

Figure 2.2:   Steam-water capillary pressure curves calculated using a scaling method for a core sample from The Geysers field.

Because the reservoir temperature of The Geysers geothermal field is greater than the test temperature, the necessary calibration for the steam-water capillary pressure due to the difference in temperature could be made using Equation 2.5.

Comparison of drainage steam-water capillary pressure. The adsorption/desorption tests used to infer capillary pressure are static processes in which there is no steam-water flow. In actual geothermal reservoirs, however, capillary pressure plays its important role while steam and water flow simultaneously through the rock. Hence the process governing an adsorption test may not represent the mechanisms under actual fluid flow conditions in geothermal reservoirs. Consequently the capillary pressures calculated using adsorption test data may or may not be the same as those measured using a dynamic method in which steam and water flow simultaneously through the porous medium. It is known that capillary pressure is influenced significantly by the contact angle. The contact angle in a static state (no fluid flow) is often different from that in a dynamic state (with fluid flow). Hence the capillary pressure is likely to be different under static and dynamic conditions. It is interesting to compare the steam-water capillary pressure data obtained using different methods.

Figure 2.3 shows the comparison of the drainage steam-water capillary pressure curve shown in Figure 2.2 with that measured in the drying process by Persoff and Hulen (1996) using an adsorption method. Note that the drainage steam-water capillary pressure data by Li and Horne (2001b) were measured at about 120°C and those by Persoff and Hulen (1996) were measured at about 28.5°C. Therefore we scaled the experimental values of steam-water capillary pressure from Persoff and Hulen (1996) to 120°C using Equation 2.5. The surface tension of steam/water at 120°C is 54.96 dynes/cm. The water saturation decreases in the drying process, which is similar to the drainage process.
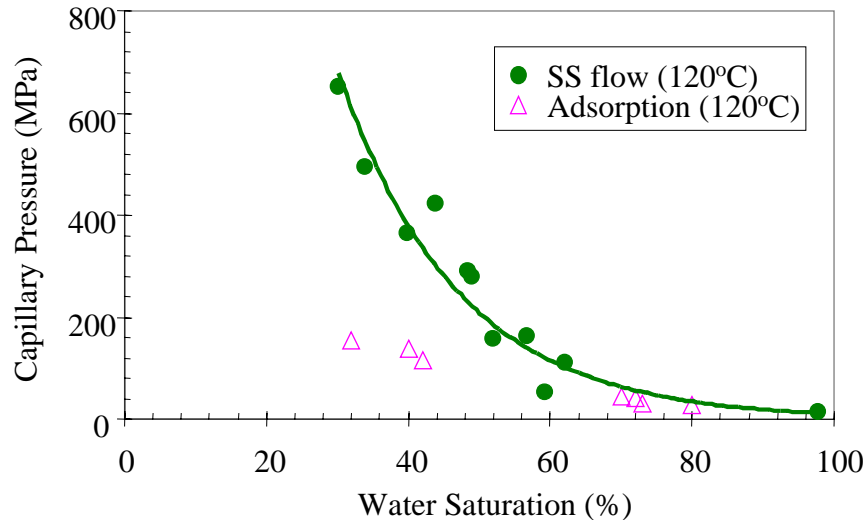

Figure 2.3:   Drainage steam-water capillary pressure curves by steady-state (SS) flow and adsorption methods for a rock sample from The Geysers field.

We can see from Figure 2.3 that the values of drainage steam-water capillary pressure measured using different methods are consistent for water saturation greater than about 60%. However the drainage steam-water capillary pressure measured using the desorption method are smaller than those measured using a steady-state flow technique for water saturation less than about 60%.

Steam-water capillary pressure model for drainage. Usually the development of a geothermal reservoir before water injection is a drainage process if there is no bottom water or aquifer and is an imbibition process otherwise. Because both drainage and imbibition processes may be involved in the development of a geothermal reservoir, steam-water capillary pressure models were developed for drainage and imbibition respectively.

The reservoir rock in geothermal fields has different porosity and permeability and it may be impossible to measure the steam-water capillary pressure for every rock sample. Therefore we need to establish a correlation between the steam-water capillary pressure of rock samples with different porosities and permeabilities.

In order to constitute such a correlation for geothermal rocks, the drainage steam-water capillary pressure data from Li and Horne (2001b) were chosen. The reason is described as follows. As we pointed out previously, there is no steam-water flow in adsorption/desorption tests, which is not a representation of the steam-water status in geothermal reservoirs in which both steam and water may be mobile. Considering this and the inconsistency between the drainage steam-water capillary pressures measured from the steady-state flow tests and those measured using adsorption approaches in some range of water saturation, we chose the data from the steady-state flow tests to constitute the steam-water capillary pressure model.

Because the drainage steam-water capillary pressure data from Li and Horne (2001b) were measured in high permeability rock, the results were scaled to the same porosity and the same permeability as used by Persoff and Hulen (1996) using Equation 2.4. The drainage steam-water capillary pressure data were plotted vs. the normalized water saturation, as shown in Figure 2.4.
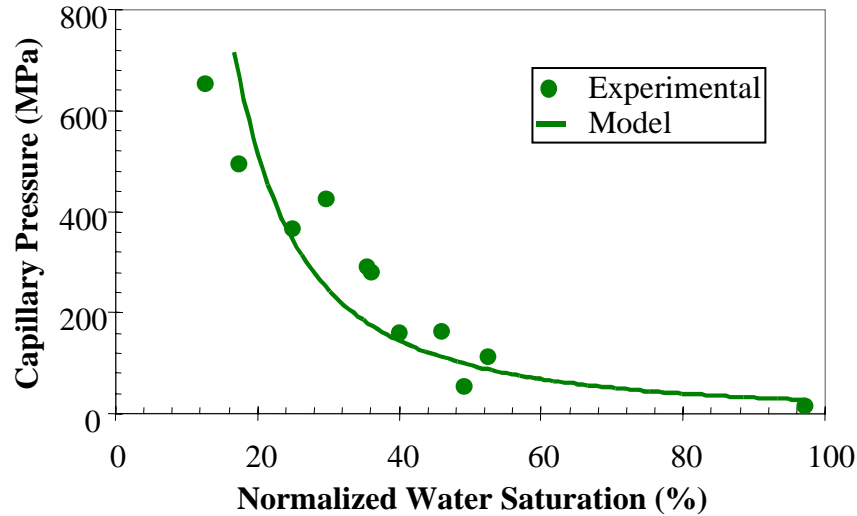

Figure 2.4:   Normalized drainage steam-water capillary pressure for a rock from The Geysers field.

The normalized water saturation is calculated using the following equation:

$$S_{wd}^* = \frac{S_w - S_{wr}}{1 - S_{wr}} \tag{2.6}$$

where S_{wr} and S_{wd}^* are the residual water saturation and normalized water saturation. The Brooks-Corey (1964) capillary pressure function is often used to model the capillary pressure curve, as given by:

$$P_c = p_e (S_{wd}^*)^{-1/\lambda} \tag{2.7}$$

37

where p_e is the entry capillary pressure and λ is the pore size distribution index. We used the Brooks-Corey capillary pressure function to fit the data. Figure 2.4 shows a match to the data scaled from Li and Horne (2001b). The values of the best-fit parameters are S_{wr} = 0.20, p_e = 26.66 MPa and λ =0.543. Note that these values are only valid when the normalized water saturation is expressed as a fraction rather than as a percentage.

Because the steam-water capillary pressures shown in Figure 2.4 were obtained from a rock sample with a permeability of about 1.3 nd and a porosity of 1.9% at a temperature of 120°C, we would need to scale the data for rocks with different porosity and permeability or for different temperatures. This can be done using Equation 2.2. Using this approach, we have created a drainage steam-water capillary pressure model based on the experimental data for geothermal rocks as follows:

$$P_c = 4.012 \frac{\sigma}{\sqrt{\dfrac{k}{\phi}}} (S_{wd}^*)^{-1.843}$$

(2.8)

where the units of P_c, σ and k are MPa, dynes/cm, and nd respectively; ϕ and S_w^* are expressed as fractions. The porosity and permeability of reservoir rocks would need to be measured. The surface tension can be calculated once the reservoir temperature is known. Therefore the steam-water capillary pressure curve for geothermal reservoir rocks may be obtained using Equation 2.8. The model expressed in Equation 2.8 is suitable for drainage process and is based on the assumptions: (1) contact angle does not change with permeability and temperature; (2) rock samples have the same J-functions.

Comparison of imbibition steam-water capillary pressure. The comparison of the imbibition steam-water capillary pressure curve measured from steady-state flow tests (see Figure 2.2) to that measured in the wetting process by Persoff and Hulen (1996) using an adsorption method is shown in Figure 2.5.
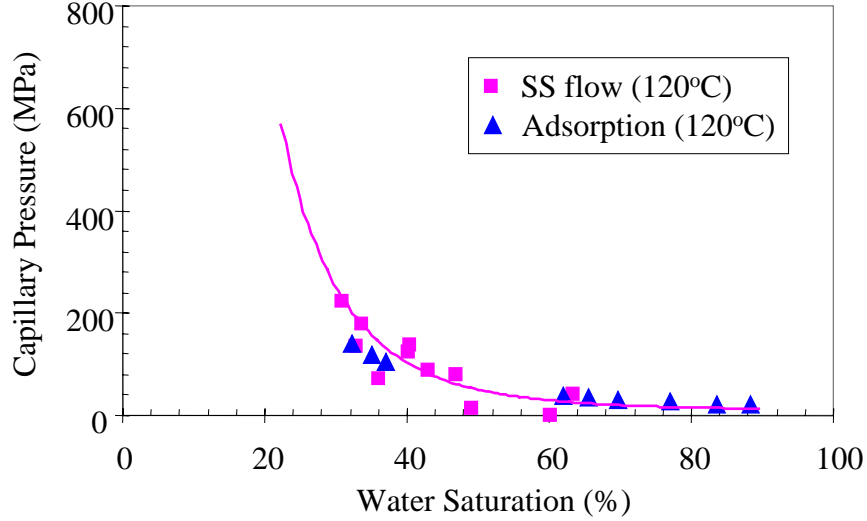
Figure 2.5:   Imbibition steam-water capillary pressure curves by steady-state (SS) flow and adsorption methods for a rock sample from The Geysers field.

The water saturation increases in the wetting process, which is similar to the imbibition process in the steady-state flow tests. The porosity and permeability of the rock sample from The Geysers geothermal field that Persoff and Hulen (1996) used were 1.9% and 1.3 nd. The imbibition steam-water capillary pressure data from Li and Horne (2001b) were measured in Berea sandstone with a higher porosity and permeability, therefore the results were scaled to the same porosity and the same permeability as used by Persoff and Hulen (1996) using Equation 2.4. Similarly, the imbibition steam-water capillary pressure data from Persoff and Hulen (1996) were measured at a temperature of 28.5^{o}C, therefore the data were scaled to the same temperature (120°C) using Equation 2.5.

We can see from Figure 2.5 that the imbibition steam-water capillary pressures obtained from the steady-state flow tests (Li and Horne, 2001b) are consistent with those measured by Persoff and Hulen (1996) after the temperature calibration. Note that this is different from the drainage case in which the two curves were different in some range of water saturation (see Figure 2.4).

Steam-water capillary pressure model for imbibition. We chose the data from the steady-state flow tests to constitute the steam-water capillary pressure model. To do so, the normalized water saturation in imbibition case is defined as follows (Li and Horne, 2001b):

$$S^*_{wimb} = \frac{S_w - S_{wi}}{1 - S_{wi} - S_{sr}} \tag{2.9}$$

where S_{wi} is the initial water saturation for imbibition; it is equal to the residual water saturation by drainage in this study. S_{sr} is the residual steam saturation by imbibition and S^*_{wimb} is the normalized water saturation for an imbibition capillary pressure model.

The Brooks-Corey capillary pressure function (Equation 2.7) was originally developed for drainage processes. Sinnokrot (1969) measured the oil-water capillary pressures of different rocks (limestones and sandstones) at different temperatures and found that the Brooks-Corey function could model the drainage oil-water capillary pressure curves but not the imbibition ones. Physically, it may not be appropriate to model imbibition capillary pressure curves using Equation 2.7. For example, there should be no parameters such as entry pressure in an imbibition capillary pressure model. Considering this, we used the imbibition capillary pressure function that we proposed previously (Li and Horne, 2001b):

$$P_c = p_m (1 - S^*_{wimb})^m \tag{2.10}$$

here p_m is the capillary pressure at S_{wi}; m is a fitting coefficient for the imbibition capillary pressure function.

The imbibition capillary pressure function expressed in Equation 2.10 was used to fit the experimental data from steady-state flow tests after scaling to the porosity of 1.9% and the permeability of 1.3 nd. Figure 2.6 shows the match between the imbibition capillary pressure function and the experimental data, given that S_{sr} is equal to 13% (Horne *et al.*, 2000). The values of the best-fit parameters are $S_{wi} = 0.20$, $p_m = 590.4$ MPa and m =5.539. Also note that these values are only valid when the normalized water saturation is expressed as a fraction rather than as a percentage.
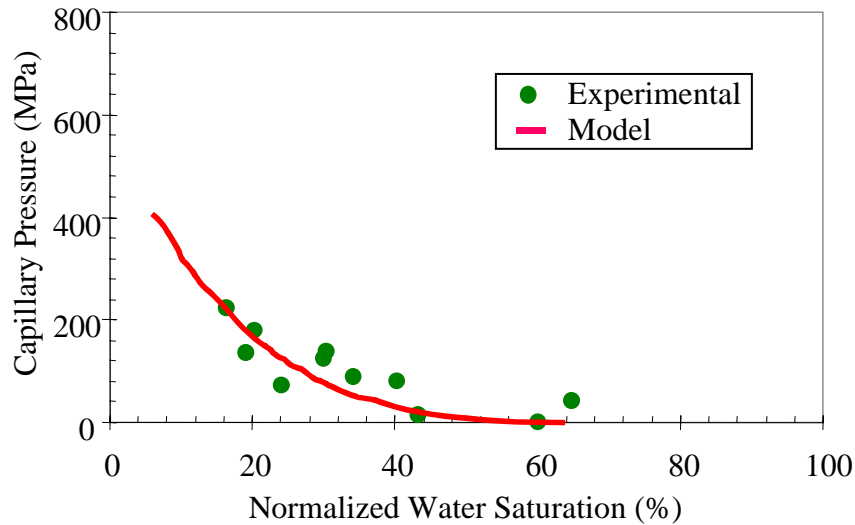

Figure 2.6:   Normalized imbibition steam-water capillary pressure for a rock from The Geysers field.

40

Using Equation 2.2 and the values obtained from fitting, we created an imbibition steam-water capillary pressure model for geothermal rock. The model is expressed as follows:

$$P_c = 88.86 \frac{\sigma}{\sqrt{\dfrac{k}{\phi}}} (1 - S_{wimb}^*)^{5.539}$$ (2.11)

where the units of P_c, σ and k are MPa, dynes/cm, and nd respectively; ϕ and S_{wimb}^* are expressed as fractions. The surface tension can be calculated once the reservoir temperature is known. Therefore, the imbibition steam-water capillary pressure curve for geothermal reservoir rocks may be obtained using Equation 2.11. The model expressed in Equation 2.11 is suitable for imbibition processes and is based on the same assumptions as the drainage model.

2.5 CONCLUSIONS

Based on the present study, the following conclusions may be drawn:
1. Both drainage and imbibition steam-water capillary pressure models have been developed for geothermal rocks based on experimental data. These models are given by Equations 2.8 and 2.11.
2. Steam-water capillary pressure in geothermal reservoirs with any porosity, permeability, and temperature can be calculated using the proposed mathematical models.
3. The scaled imbibition steam-water capillary pressure from a steady-state flow technique is consistent with that measured by an adsorption method. However the drainage results from the two approaches are not consistent in some range of water saturation.

3. FRACTURED ROCK RELATIVE PERMEABILITY

This project is being conducted by Research Assistant Mark D. Habana, Senior Research Engineer Kewen Li and Prof. Roland N. Horne. The objective is to measure relative permeability relations for nitrogen and water flow in a fractured geothermal rock. This work is an extension of current studies of nitrogen-water and steam-water flows, which have so far considered only artificially uniform porous rock. The project was completed this quarter and a technical report prepared.

3.1 BACKGROUND

Relative permeability is one of the most uncertain terms in equations of multiphase fluid flow through porous and fractured media. Such a basic parameter must be well understood to have confidence in reservoir simulations and other models of fractured media that are based on these equations.

Much work has been done dealing with flow properties in nonfractured porous media. Increased understanding of flow behavior in fractures will allow more realistic models. This work aimed to determine nitrogen-water relative permeability relations for a fractured geothermal rock from The Geysers.

Various works on flow through fractures have shown different kinds of relative permeability behavior. Experimental studies by Persoff and Pruess (1995) resulted in curves that can not be classified either as Corey type or as linear (X-curve) type. Fourar et al. (1993) suggested that multiphase interaction in a fracture is a function of flow velocity and, therefore, relative permeability is not the appropriate way to describe multiphase flow in fractures.

Past experiments have used synthetic fabricated fractures and/or gas-water or oil-water as fluids. This experimental study used a real fractured rock core from The Geysers geothermal field to study nitrogen-water relative permeability.

Understanding nitrogen-water relative permeability through fractures will provide valuable information prior to the next challenge: steam-water relative permeability.

3.1.1 Darcy's Law and Slip Factors

One-dimensional flow through porous media is described by Darcy's law.

$$q = \frac{k_{abs} k_r A}{\mu} \frac{\Delta p}{\Delta x} \qquad (3.1)$$

where q is the volumetric flowrate

k is the absolute permeability

k_r is the relative permeability

A is the cross sectional area of flow

μ is the fluid viscosity

$\Delta p/\Delta x$ is the pressure gradient

For isothermal flow of an ideal gas Darcy's law is modified as Equation (3.2).

$$q_{mean} = \frac{k_{abs}k_r A}{\mu}\frac{\Delta p}{\Delta x}$$ (3.2)

where q_{mean} is the volume flowrate at the mean pressure

The Klinkenberg effect is observed for gas flows wherein the absolute permeability calculated using Darcy's equation is greater than the real absolute permeability. The slip factor is introduced to correct for this difference.

$$k_{abs} = \frac{k_{gas}}{(1-\dfrac{b}{p_{ave}})}$$ (3.3

where b is the slip factor

p_{ave} is the average of the inlet and outlet pressures

k_{gas} is the uncorrected permeability

k_{abs} is the absolute permeability

The value of the slip factor is obtained by plotting the gas permeability values versus the reciprocal of different mean pressures. Extrapolating the curve to the y-axis gives the correct value of absolute permeability. Dividing the slope by the y-intercept of the equation of the extrapolated line gives the slip factor.

3.1.2 Relative Permeability Curves

Corey curves are observed often in homogeneous porous media while X-curves are typically assumed for fracture flows.

The Corey and X-curves are modeled by the equations below.

Corey Curves:

$$k_{rl} = S^{*4} \qquad\qquad (S^* < 1)$$ (3.4)

$$k_{rl} = (1 - S^*)^2 (1 - S^{*2}) \qquad (S^* < 1)$$ (3.5)

$$S^* = \frac{(S - S_{lr})}{(S_{gr} - S_{lr})}$$ (3.6)

X-curves:

$$k_{rl} = S^* \qquad\qquad (S^* < 1)$$ (3.7)

$$k_{rl} = (1 - S^*) \qquad\qquad (S^* < 1)$$ (3.8)

$$S^* = \frac{(S - S_{lr})}{(S_{gr} - S_{lr})}$$ (3.9)

where k_{rl} is the relative permeability of the liquid and k_{rg} is the relative permeability of the gas. S_{lr} is the irreducible water saturation and S_{gr} is the water saturation at irreducible nitrogen gas saturation.

3.1.3 Resistivity

Experiments by Archie(1942) showed a relationship between resistivity and saturation. Resistivity is the reciprocal of conductivity, or the ability of a material to allow flow of current.

$$\rho = r\left(\frac{A}{L}\right)$$ (3.10)

where r is resistance

A is area

L is length

ρ is resistivity

Archie's equation relates the resistivity index to the water saturation.

$$R_{index} = S_w^{-2}$$ (3.11)

$$R_{index} = \rho_t / \rho_o$$ (3.12)

where R_{index} is the resistivity index

ρ_t is the resistivity of the core with less than 100% water saturation

ρ_o is the resistivity of the core at 100% water saturation

Thus, knowing R_{index} the water saturation, S_w, can be computed.

3.2 EXPERIMENT METHODOLOGY

Several preliminary experiments and flow simulations were conducted prior to the nitrogen-water relative permeability experiments. These were done to determine issues involved in conducting the experiment on a fractured rock.

3.2.1 Absolute Permeability

Nitrogen and Helium Experiments

The core sample was obtained from a depth of 1409.3 m at The Geysers geothermal field. The core is 6.91 cm in diameter and 4.70 cm in length.

The rock permeability was measured using nitrogen and helium gas at room temperature. Since gas permeability is a function of pressure, as described by Equation 3.3, the flow measurements were conducted at a series of different mean pressures.

At different confining pressures nitrogen was flowed through the core. Confining pressure from 500 to 850 psig was applied by injecting nitrogen around the heat shrink

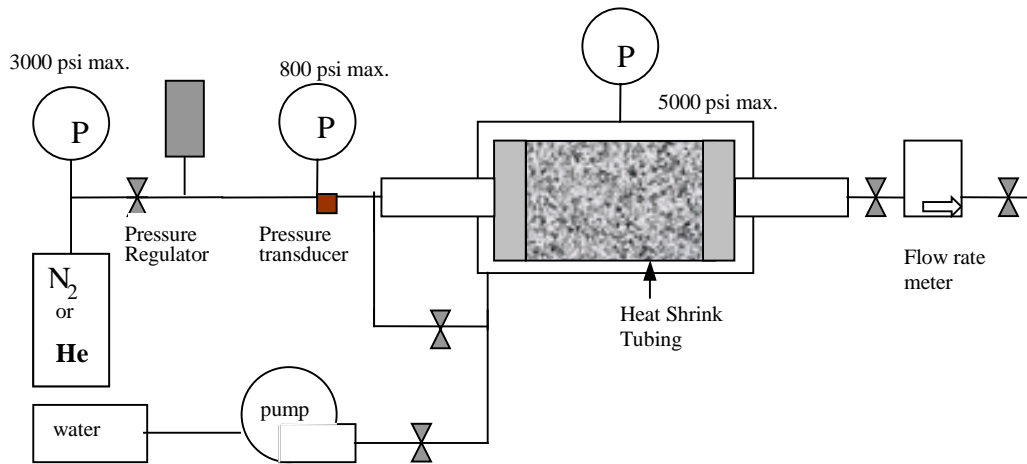tubing inside the core holder. To apply a confining pressure of 1150 psig water was used in place of nitrogen.

Figure 3.1: Apparatus for flow measurement in geothermal rock.

A pressure gauge and a pressure transducer connected to a digital display measured pressure at the inlet. The pressure at the outlet was taken to be 1 atm. The flow rate at the outlet was measured using a Matheson flow rate meter and controller (Model 8272-MF2000). The flow rate transducer calibration equation used was that determined by Kewen Li when he used the device in his experiments on slip factors (Oct-Dec 1999 Quarterly Report).

Nitrogen absolute permeability experiments were also conducted on another core. This core, with a diameter of 5.08 cm (2") and a length of 4.445 cm, was cut from The Geysers geothermal rock obtained at a depth 1450 meters. This 2" diameter core was made so a standard rubber sleeve could be used instead of the heat shrink tubing.

Three nitrogen experiments were completed for the 2" diameter core. The first one was conducted after drying the newly cut core and the second after performing several nitrogen-water relative permeability experiment runs.

The third nitrogen experiment was done under constant net stress. The net stress was controlled by reducing (or increasing) the confining pressure by the same amount as the decrease (or increase) of the inlet and outlet pressures. The pressure difference between the inlet and outlet was maintained constant.

Water Injection Experiments

Four water injection experiments were conducted on the 2" diameter core. The first was conducted after vacuuming the core; after the first nitrogen absolute permeability experiment. The flowrate was maintained constant at 10 ml/min. Steady state was

deemed achieved when the pressure at the inlet was relatively constant. The outlet pressure was maintained at atmospheric pressure.

The other three water injection experiment runs were done after the second nitrogen absolute permeability experiment. Different water flowrates were used in the three runs: 14 ml/min, 10 ml/min, and 0.1 ml/min.

The water pump maximum outlet pressure was set to 800 psig. This was done to prevent pressure in the core from exceeding the confining pressure of 850 psig.

3.2.2 Resistivity Experiments

Two resistivity experiments were done using a disc-shaped homogeneous rock. The same experiment was done also using a heterogeneous rock. The apparatus is shown in Figure 3.2.
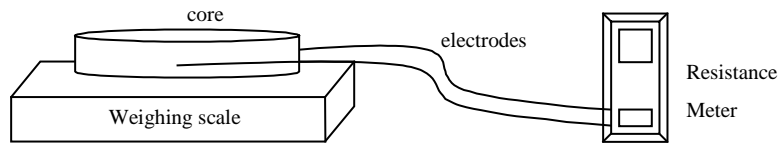

Figure 3.2 Apparatus for resistivity experiments.

The core was saturated fully with water and then allowed to dry on a weighing scale. Resistance measurements were measured for every 1 gram decrease in mass of the saturated core. Resistivity and resistivity indices were calculated for each resistance reading by using Equation 3.10, Equation 3.11 and Equation 3.12.

To determine the resistivity-saturation correlation for the 2" diameter Geysers core the apparatus shown in Figure 3.3 was used.
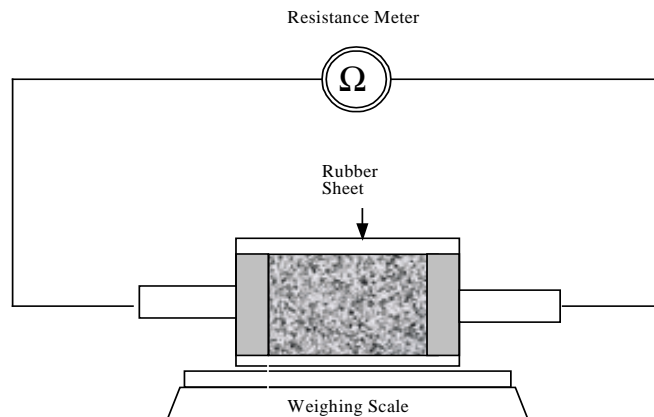

Figure 3.3: Apparatus for determining resistivity-saturation correlation in geothermal rock.

The core was fully saturated with water and then wrapped with rubber sheet, with the two metal plates attached on both ends of the core. The core was then allowed to dry on a weighing scale. Resistance measurements were measured as the mass of the saturated core decreased.

The resistance meter has a maximum resistance reading of 40MΩ. To be able to measure resistances higher than 40MΩ several resistors and rheostats in series connection were assembled. Connecting these resistors to the core in parallel caused the overall resistance to decrease below 40MΩ. The core resistance was then computed using the basic equation for parallel resistances.

3.2.3 Nitrogen-Water Relative Permeability

Eclipse Simulation

Flow simulations were done to determine whether uniform saturation could be achieved in the core and to estimate the amount of time required to achieve steady state.

The cylindrical core was modeled as a rectangular reservoir. Grid block parameter values were 4.3% for porosity and 0.5 md for permeability. The Eclipse simulation code used is listed in Appendix A of Habana (2002).

Relative Permeability at Endpoint Saturations
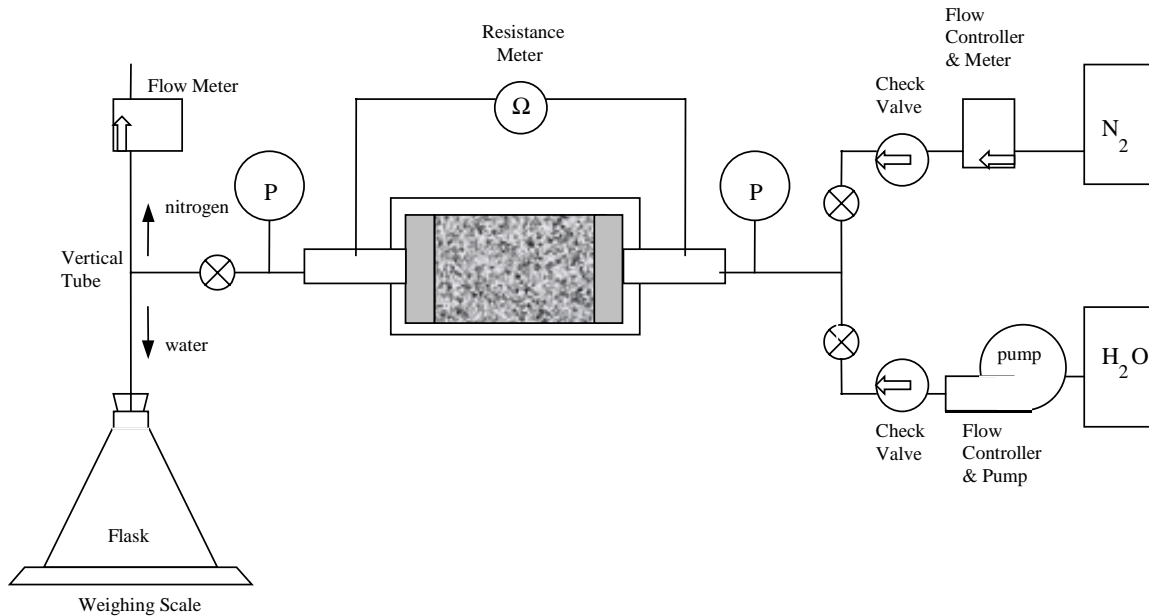

Figure 3.4: Apparatus for nitrogen-water relative permeability experiment.

The experiments had inlet flow controls of constant nitrogen gas pressure and constant water flowrate. The data acquisition system was automated using a PCI-6024E board and an SCB-68 shielded connector block; both manufactured by National Instruments. Resistance measurements were taken at the end of the experiment runs for use in

determining the water saturation. The metal stems of the core endplates were covered with Torlon plastic to isolate the core electrically from the core holder.

During relative permeability experiments at irreducible water saturation the nitrogen gas injected was made to pass through a cylinder containing water. This was done to saturate the gas with water.

Two sets of endpoint saturation relative permeability experiments were completed. Each set includes an experiment at irreducible water saturation and another experiment at irreducible nitrogen saturation.

Nitrogen and Water Injection

Several nitrogen-water relative permeability experiment runs were done. Initially, the inlet flow control was at constant flowrate for both nitrogen and water. Later experiments controlled the inlet pressure of nitrogen and the inlet flowrate of water.

Five constant flowrate nitrogen-water relative permeability experiments were completed. Difficulties in achieving steady state were encountered and, thus, the experiment was changed to constant nitrogen gas pressure and constant water flowrate.

3.3 RESULTS AND DISCUSSION

3.3.1 Absolute Permeability

Nitrogen and Helium Experiments

Results of the nitrogen experiments on the 6.91 cm diameter core are shown in Figure 3.5. The intersection of the extrapolated lines with the vertical axis in the plot of permeability (k) versus the reciprocal of the mean pressure ($1/p_{ave}$) is taken to be the absolute permeability of the rock. The values of permeability range between 0.22 and 0.38 md.

It was observed that for the nitrogen experiments the permeability values decrease with increasing confining pressure. This can be attributed to the increase in net stress on the rock fractures as the confining pressure is increased. The increased net stress reduces the fracture aperture and, consequently, reduces the permeability.

There is a linear relationship between confining pressure and the absolute permeabilities obtained by extrapolation. This is shown in Figure 3.6.
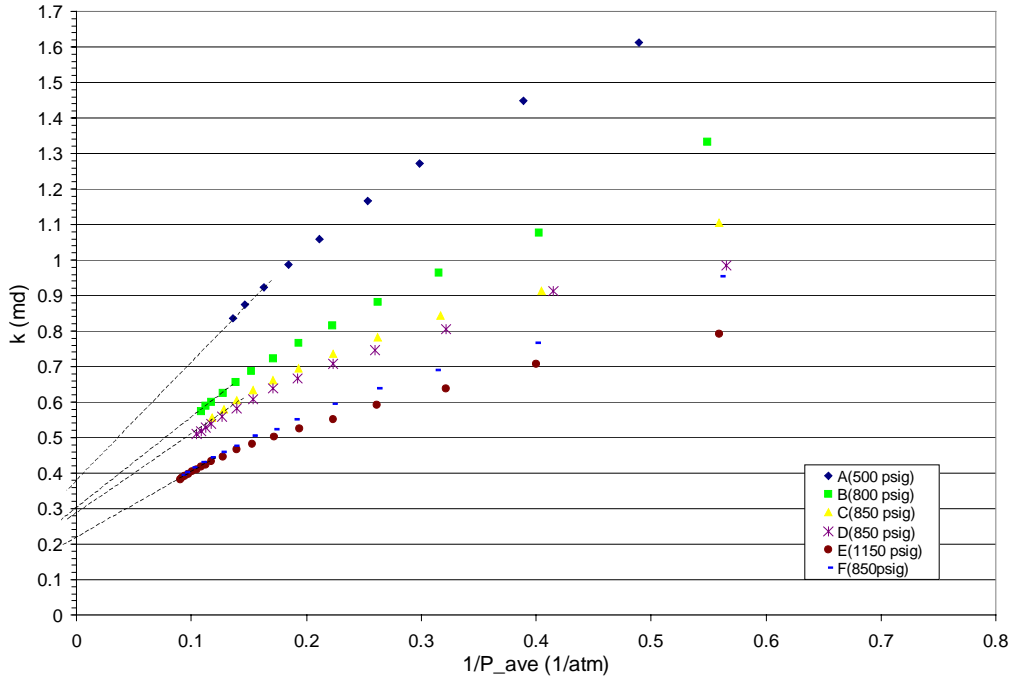
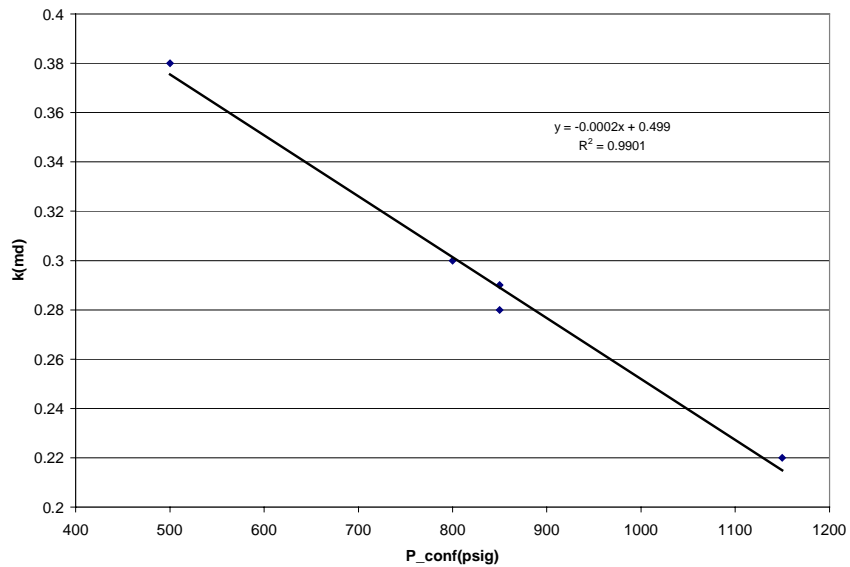*Figure 3.5: Results of nitrogen and helium permeability as a function of pressure.*

Figure 3.6: Absolute permeability results from nitrogen experiments.

Figure 3.7 and 3.8 show two helium experiment results compared to the two nitrogen experiments preceding each helium experiment. All four flow experiments were done at a confining pressure of 850 psig. For the helium experiment the permeabilities obtained are higher than the values from the nitrogen experiments. Also, the slope for the helium experiment is lower than that for nitrogen at high confining pressures. This is not as

expected. The slope for helium should be much steeper than that for nitrogen considering the difference in viscosities and molecular weights of the two fluids.
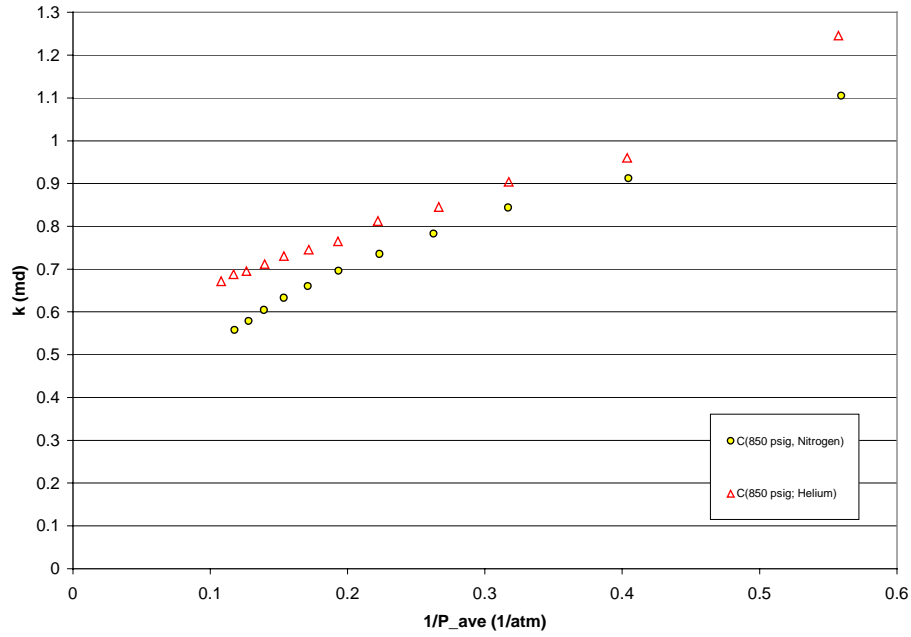

Figure 3.7: Results of helium and nitrogen permeability as a function of pressure. From experiment C.
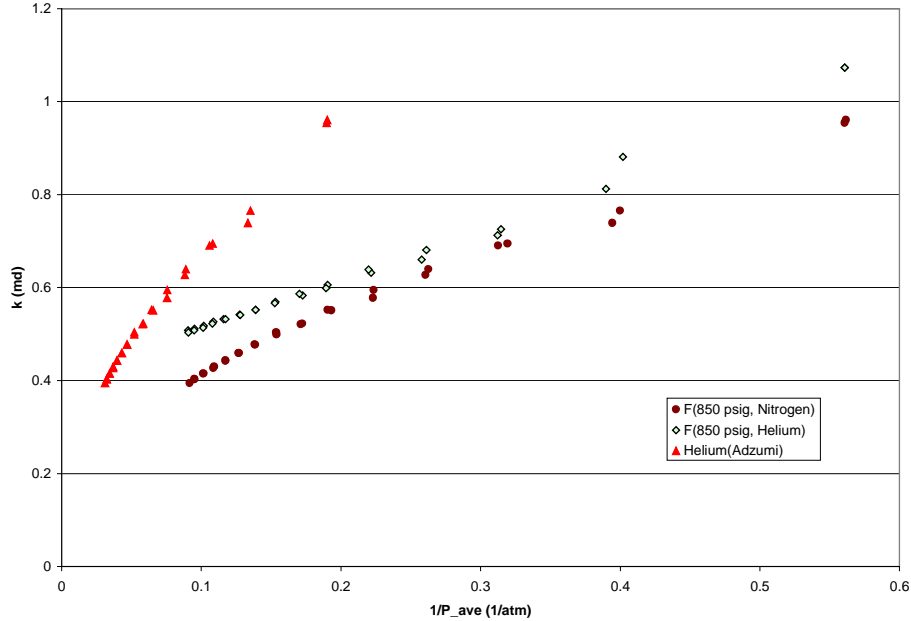

Figure 3.8: Calculated helium permeability values using Adzumi's equation and results of helium and nitrogen permeability as a function of pressure. From experiment F.

Assuming that the nitrogen data in Figure 3.8 is correct we can calculate the helium permeabilities for a porous media using Adzumi's equation, Equation 3.13.

$$\frac{p_2}{p_1} = (\frac{\mu_2}{\mu_1})\sqrt{T_2 M_1 / T_1 M_2}$$

(3.13)

k_g(gas 1 at p_1 and T_1) = k_g(gas 2 at p_2 and T_2)

where p is pressure

T is temperature

μ is viscosity

subscripts 1 and 2 determine the gas

The calculated helium permeability values are shown as triangles in Figure 3.8. This implies that the permeability for a porous core is higher than that for a fractured core. Viscosity and molecular weight effects were investigated but were not able to provide an explanation for the discrepancies observed. It was found that helium was at supercritical conditions during the entire experiment. The critical pressure of helium is 2.2449 atm and its critical temperature is –267.95 ^{o}C. This critical pressure corresponds to a value of the reciprocal of mean pressure of 0.616. Ordinary flow equations, therefore, do not apply to the helium data obtained. Nitrogen, on the other hand, is at subcritical conditions. The critical point of nitrogen is at 33.514 atm and –146.958 ^{o}C.

Nitrogen experiments at a confining pressure of 850 psig were also conducted on the 2" diameter core. Experiment H was done prior to nitrogen experiments K and L. The absolute permeability value obtained from Experiment H is 0.6 md. This is twice the absolute permeability of the 6.91 cm diameter core. This is due to the large fracture that cuts across the 2" diameter core at an angle of approximately 45 degrees relative to the core axis. Figure 3.9 shows the data for the three experiments.

Experiment L was done after several nitrogen-water relative permeability experiments. The results show a decrease in the absolute permeability from 0.6 md to 0.35 md. Other researchers observed similar phenomena. Work by Bandis et al. (1981) showed that natural geological joints decrease in aperture as the number of loading cycles increase. Also, Myer (1991) measured flowrate change in metal casts of natural fractures and observed a decrease in flowrate due to an increase in number of loading cycles. This can be explained by the destruction and/or deformation of the fracture asperities causing the aperture to decrease.
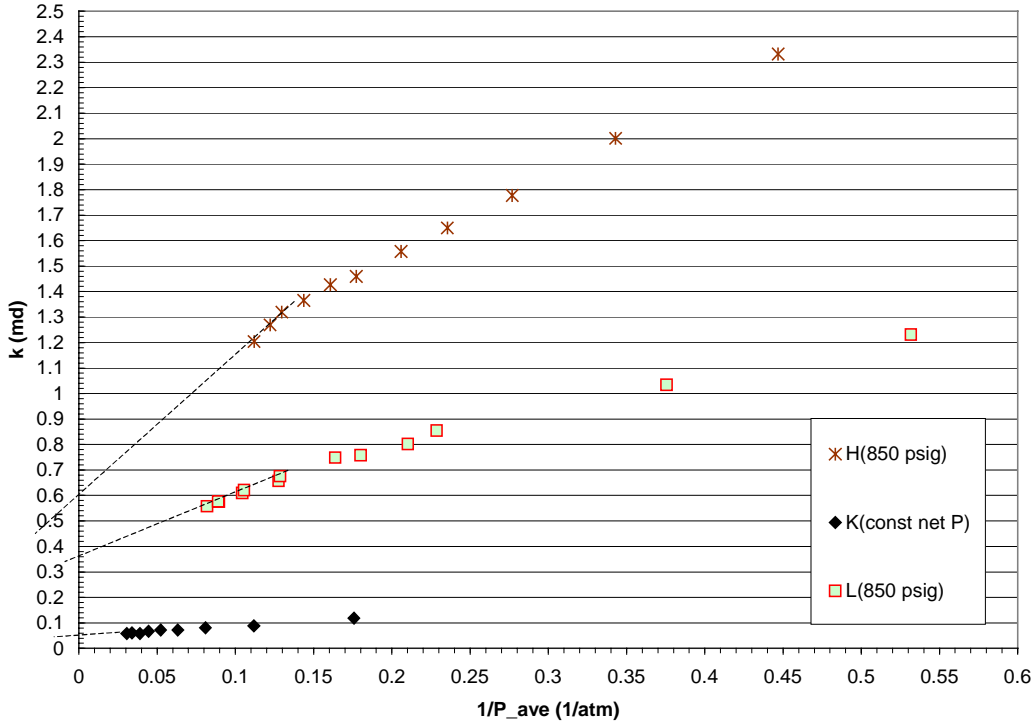
Figure 3.9: Nitrogen experiment results for the 2" diameter core.

Considering the effect that the net effective stress has on the fluid flow an experiment, labeled L, was done at constant net normal stress. The result plots as a straight line on the *k* vs. *1/p$_{ave}$* axes and does not show the curvature at high confining pressures observed in the previous experiments. Experiment L gives an absolute permeability value of 0.048 md. This is very low and is unlikely to be correct because the experiment does not maintain the shear stresses on the core. As the confining pressure is changed the pressure on the core endplates also changes. Shear stress changes will cause asperities to position within voids causing a significant decrease in the flow path area. Figure 3.10 shows normal and shear stress orientations relative to a fracture surface.
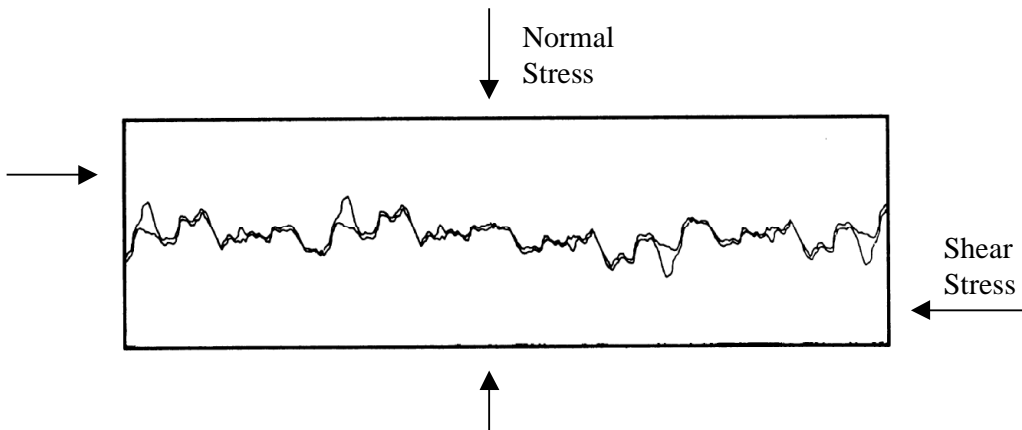

Figure 3.10: Schematic of a fracture surface. From Rock Fractures and Fluid Flow *by the Committee on Fracture Characterization and Fluid Flow, National Research Council.*

Table 3.1: Absolute permeability and slip factor values from nitrogen experiments.

Experiment	Confining Pressure (psig)	Absolute Permeability (md)	Slip Factor (atm)	Remarks
A	500	0.38	9.091	6.91 cm dia. core
B	800	0.3	8.859	6.91 cm dia. core
C	850	0.29	7.356	6.91 cm dia. core
D	850	0.28	7.619	6.91 cm dia. core
E	1150	0.22	8.182	6.91 cm dia. core
F	850	0.22	8.182	6.91 cm dia. core
H	850	0.60	9.091	5.08 cm dia. core
K	variable	0.048	7.906	5.08 cm dia. core, constant normal net P
L	850	0.35	7.143	5.08 cm dia. core

Water Injection Experiments

Prior to the relative permeability experiments the absolute permeability was obtained by injecting water into the dried and vacuumed 2" diameter core. Flowrate was maintained constant at 10 ml/min. Inlet pressure measurements are shown in Figure 3.11.
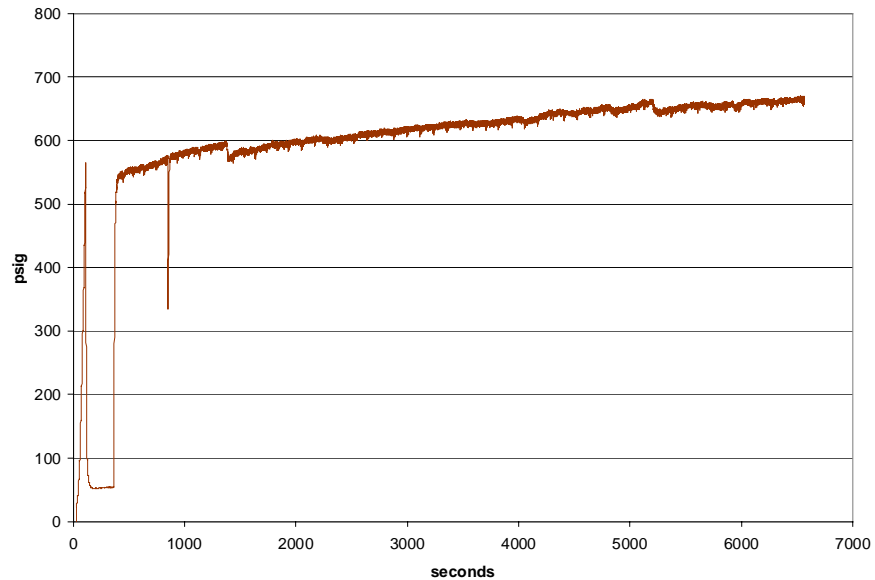

Figure 3.11: Pressure at inlet during water injection. Constant water flowrate at 10 ml/min.

The calculated absolute permeability, using an inlet pressure of 669 psig and an outlet pressure of 11 psig, is 0.808 md.

The pore volume and porosity were obtained by weighing the core after this experiment. The pore volume is 3.87 cm^3 and the porosity is 4.3%.

Another absolute permeability experiment using water was done after several relative permeability experiment runs. Figure 3.12 shows the inlet pressure data for this experiment.

The inlet pressure demonstrates regularly occurring up and down cycles. The rise in each cycle is abrupt while the fall is relatively slow. The water pump does not cause the sudden rise because the recharge timing of the positive displacement pump is much shorter than the timing of the pressure spikes.
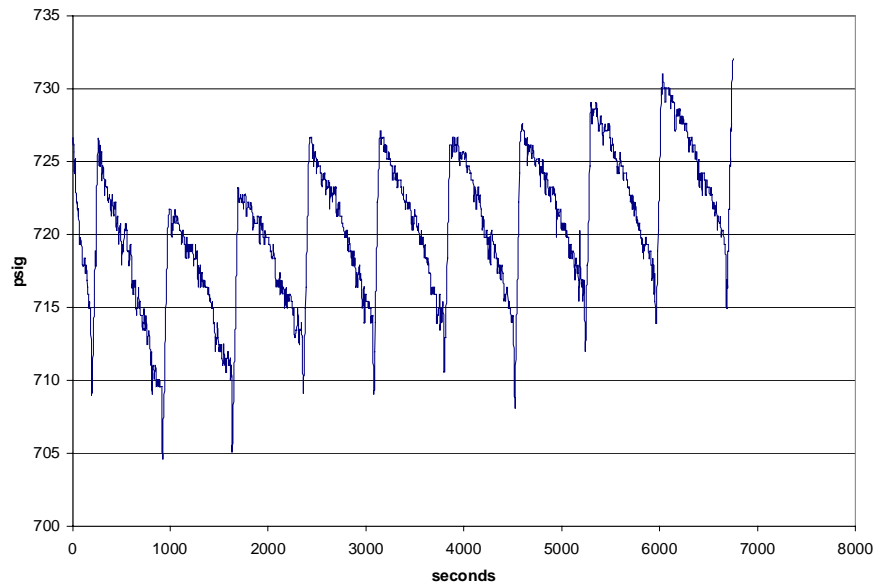

Figure 3.12: Pressure at inlet during water injection. Constant water flowrate at 14 ml/min.

A conceptual model of fracture networks, assuming elastic rock fracture behavior, could provide an explanation. Water flows preferentially through the large fractures in the rock. In the case of the experiment, water was pumped at high pressure and high flowrate. This causes small fractures to stay open. However, pressure drops because the rock matrix and fracture network are capable of allowing more than 14 ml/min of fluid flow. When a certain low pressure is reached the small fractures close causing the sudden rise in pressure. The pump maintains a constant flowrate and will provide the required pressure that will reopen the small fractures. It is not necessary for many small fractures to close and open simultaneously. One small fracture may be the only link to a subset of fractures in the fracture network.

The drops in pressure are not likely due to fracture propagation/initiation because the absolute permeabilities obtained from the nitrogen experiments decreased as more

experiments were conducted on the core. This suggests that fracture propagation has not occurred and if it has only to a degree much less significant than fracture aperture changes due to destruction of asperities.

The core is known to be heterogeneous (i.e. contains veins) and this causes discontinuous fracture propagation at the interface of different rock materials, Figure 3.13. Discontinuous fracture propagation is known to be the preferential mechanism of fracture initiation induced by another fracture in the adjacent material. This hinders the creation of connected fracture networks even if the rock is subjected to high stresses. Continued application of load cycles will later cause these fractures to connect. This connection of fractures may have occurred in Experiment 2 of the nitrogen-water relative permeability experiment.
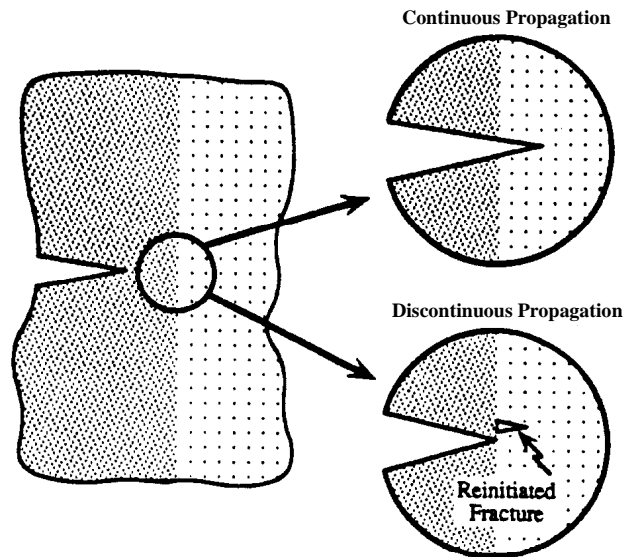

Figure 3.13: Continuous vs discontinuous propagation across interface of two rock materials. From Renshaw and Pollard (1995).

The general pressure trend in Figure 3.12 is increasing. There are several possible reasons for this. The effect may be due to swelling clays and/or strain hardening of the fractures. Fines may also be accumulating.

Since steady pressures were not achieved at 14 ml/min the flowrate was reduced to 2 ml/min. The inlet pressure measurements are shown in Figure 3.14.

The fracture network model discussed previously can be used to explain the inlet pressure behavior for the 2 ml/min experiment. The low flowrate causes the pressure rise to be slower than the fall in pressure. At high inlet pressures, the fractures are not very stable because the low net stress and low flowrate is not enough to maintain the fracture openings. Thus, pressure fluctuations at 700 psig and above are observed. Again, fines may also be the culprits causing the fluctuations.
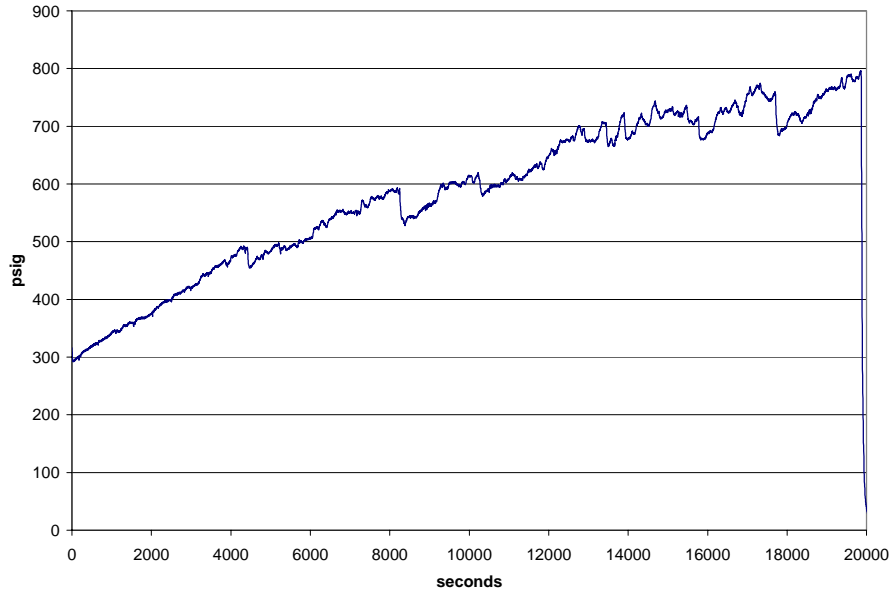
Figure 3.14: Pressure at inlet during water injection. Constant water flowrate at 2 ml/min.

Water at the outlet was filtered to determine if fines were being produced. No fines were found. This does not eliminate the possibility that some fines were trapped within the core.

Steady state was not achieved because the pressure reached the maximum pump pressure limit. Due to this the flowrate was reduced further to 0.1 ml/min.

The inlet pressure data of the water injection experiment at 0.1 ml/min is shown in Figure 3.15. After three days, the pressure still had not reached steady state. Cycles of slow pressure rise and sudden drops similar to the 2 ml/min experiment were observed.

To get a sense of what is happening with the rock, calculations of absolute permeability were made at pressures that are judged to be relatively stable.
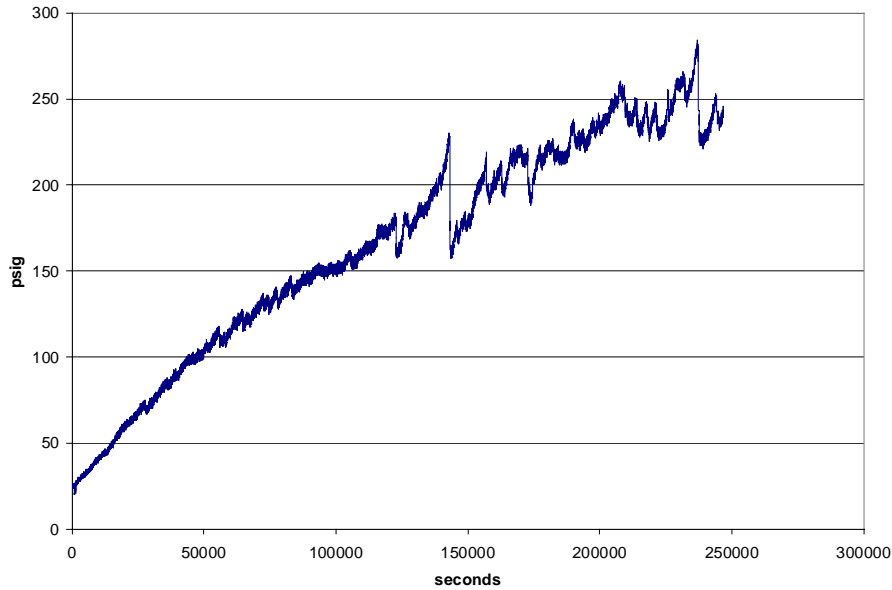
Figure 3.15: Pressure at inlet during water injection at constant water flowrate of 0.1 ml/min.

Table 3.2: Absolute permeability values from water injection experiments.

Experiment	Flowrate (ml/min)	Stable Pressure (psig)	Absolute Permeability (md)
1	10	668	0.8082
2	14	730	1.0445
3	2	730	0.1492
4	0.1	230	0.0244

3.3.2 Resistivity Experiments

Resistivity measurements were used to determine the average water saturation in the core. Experiments were conducted on two disc-shaped rocks before establishing the resistivity-saturation relationship for the 2" diameter core.

Resistivity experiments on the disc-shaped homogeneous rock showed a linear relationship between R_{index} and saturation in a log-log plot, Figure 3.16. Series 1 and Series 2 are different experiments on the same rock sample. This is very similar to the result obtained by Archie (1950). For the heterogeneous rock, resistance readings were only obtained for a saturation range of 1 to 0.76, Figure 3.17. This is due to water drying out at the point of contact of the electrodes while most of the water is concentrated in the visible fractures of the core. This is a challenge in the application of the resistivity technique to saturation measurements in heterogeneous rocks.
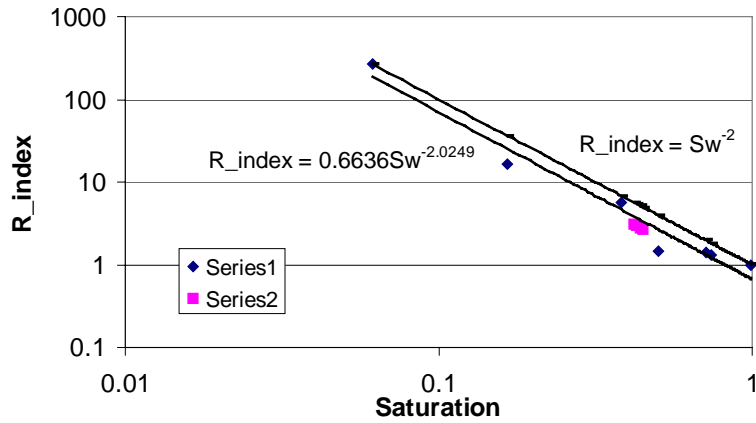
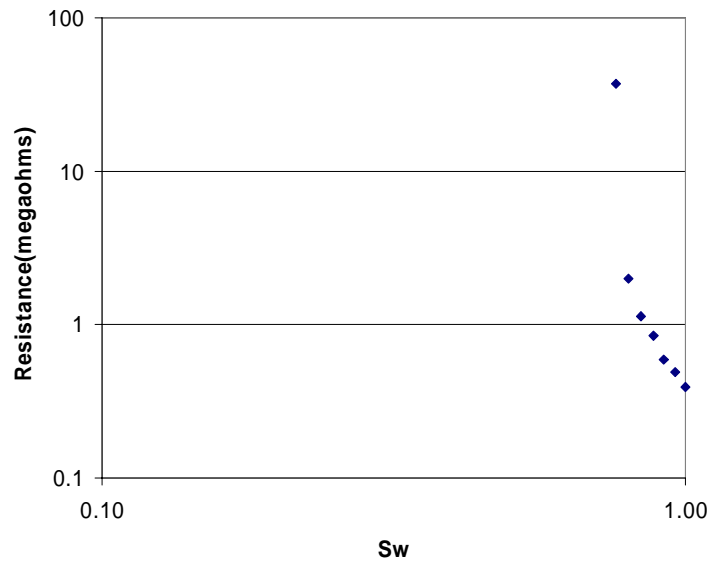*Figure 3.16:* R_{index} *versus water saturation for homogeneous rock.*

Figure 3.17: Resistance versus water saturation for heterogeneous rock.

To overcome the difficulty in measuring resistance at low water saturations several resistors and rheostats were connected in parallel with the core, thereby reducing overall resistance below the resistance meter limit of 40 MΩ. The result of the resistivity experiment on the 2" diameter core is shown in Figure 3.18.

The water saturation of the core was then determined by the equation,

$$S_w = \left(\frac{0.7855}{R\_index} \right)^{\frac{1}{3.7589}}$$ (3.14)
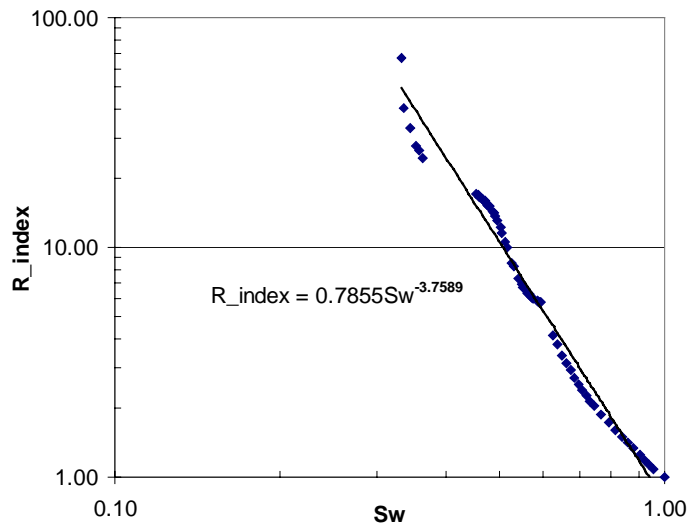
Figure 3.18: Resistance versus water saturation for 2" diameter core from The Geysers.

The irreducible water saturations were obtained after nitrogen experiments H and L. The irreducible nitrogen saturations were determined upon completion of water injection experiments conducted after nitrogen experiments H and L.

Table 3.3: Irreducible water saturation.

Nitrogen Experiment	Weighing Method	Resistivity Method
Experiment H	12.9%	15.43%
Experiment L	17.57%	14.3%

Table 3.4: Water saturation at irreducible nitrogen gas saturation.

Water Injection Experiment	Weighing Method	Resistivity Method
Experiment 1	79.1%	78.76%
Experiment 2	78.55%	80.89%

The irreducible water saturation is approximately 15% and the irreducible gas saturation is about 20%. Evaporation has a bigger effect on the measurements done at irreducible gas saturation than at irreducible water saturation because more water is exposed to the atmosphere. This may cause lower mass readings for the core at irreducible nitrogen saturation. Therefore, the water saturation at irreducible nitrogen gas saturation may be higher than the values in Table 3.4.

The resistivity readings provide acceptable values and can be used to give saturation estimates for similar experiments.

3.3.3 Nitrogen-Water Relative Permeability

Eclipse Simulation

Flow simulations were done using Eclipse to determine the saturation distribution behavior in the core when nitrogen and water are injected simultaneously. Also, the simulation provides estimates of the time required to achieve steady state. Injection flowrates were controlled in the different simulations. Nitrogen and water were injected at the middle block of the left face of the core model and produced at the middle block of the right face.

Matrix porosity of 4.3% and permeability of 0.5 md were used. The fracture was simulated by a double porosity model where the fracture was given a porosity of 100%.
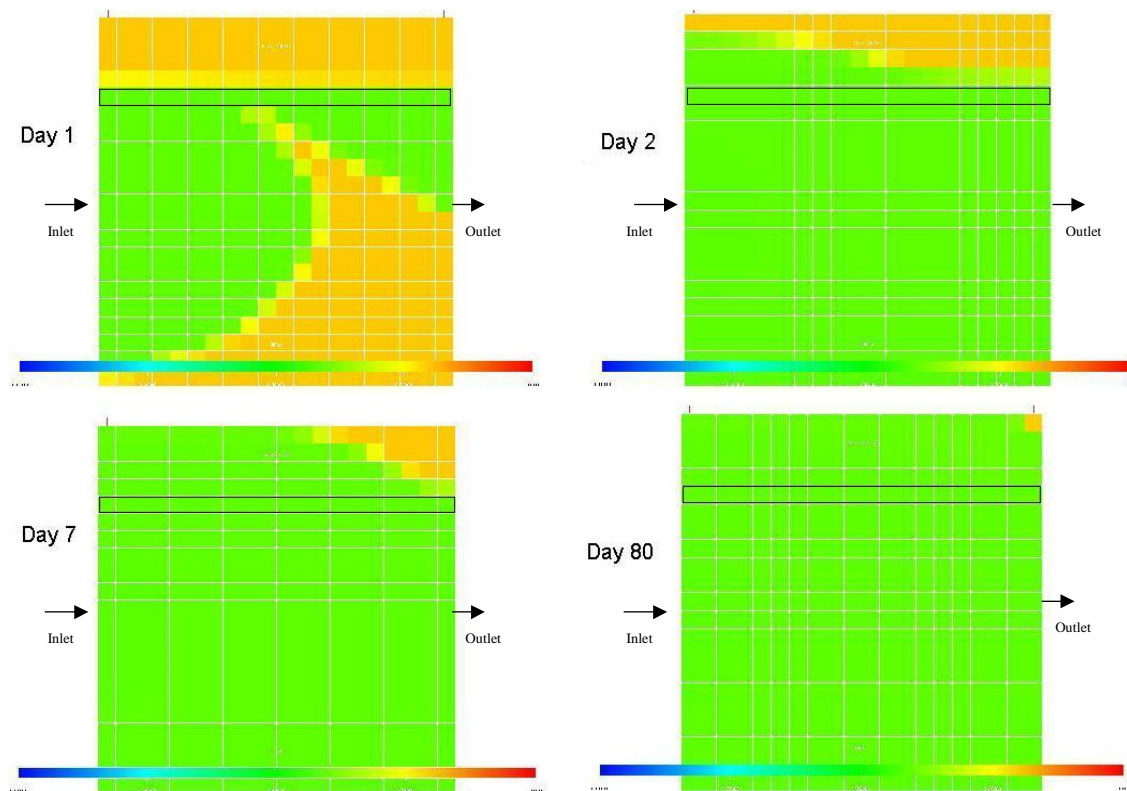

Figure 3.19: Saturation map for imbibition with horizontal fracture connecting left and right faces of the core model. Fracture is indicated by the black rectangle.

Steady-state uniform saturation was attained in approximately 80 days as shown in Figure 3.19. Red in the graduated color scale indicates 100% nitrogen gas saturation and blue indicates 100% water saturation.

A single fracture or a fracture network that horizontally connects the left and right faces of the core may not be the case for the 2" diameter core used in this study. Thus, further

simulations were done for an inclined fracture and for a horizontal fracture that does not extend completely from the left to the right faces of the core model.

For simulations with a short horizontal fracture, located in the upper middle of the core, steady-state uniform saturation was reached in less than 10 hours. This is shown in Figure 3.20.

Simulations with an inclined fracture extending from the left to the right of the core achieved steady state in 20 hours, Figure 3.21.

Other drainage and imbibition simulations at different gas and water injection flowrates that were done all reached steady state in less than 24 hours.

Therefore, for an ideal fractured core, steady-state uniform saturation can be realized in 24 hours or less. An ideal fractured core will have no clay swelling, fines, and fracture networks that connect the left and right faces of the core horizontally.
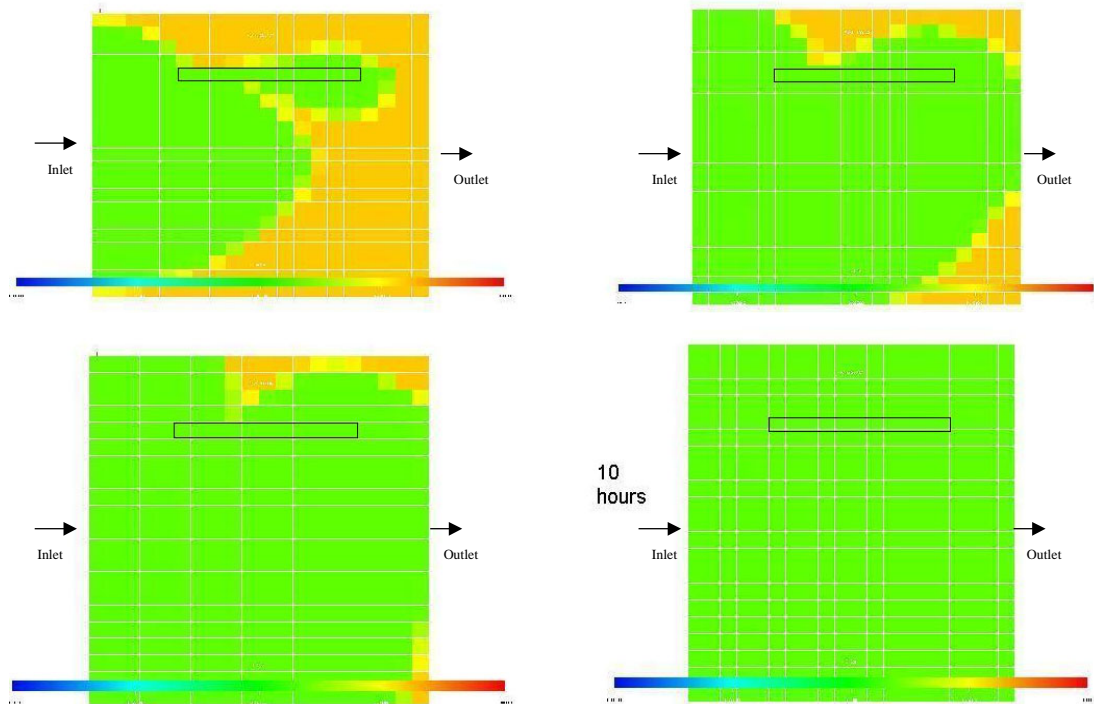

Figure 3.20: Saturation map for imbibition with short horizontal fracture. Fracture is indicated by black rectangle.
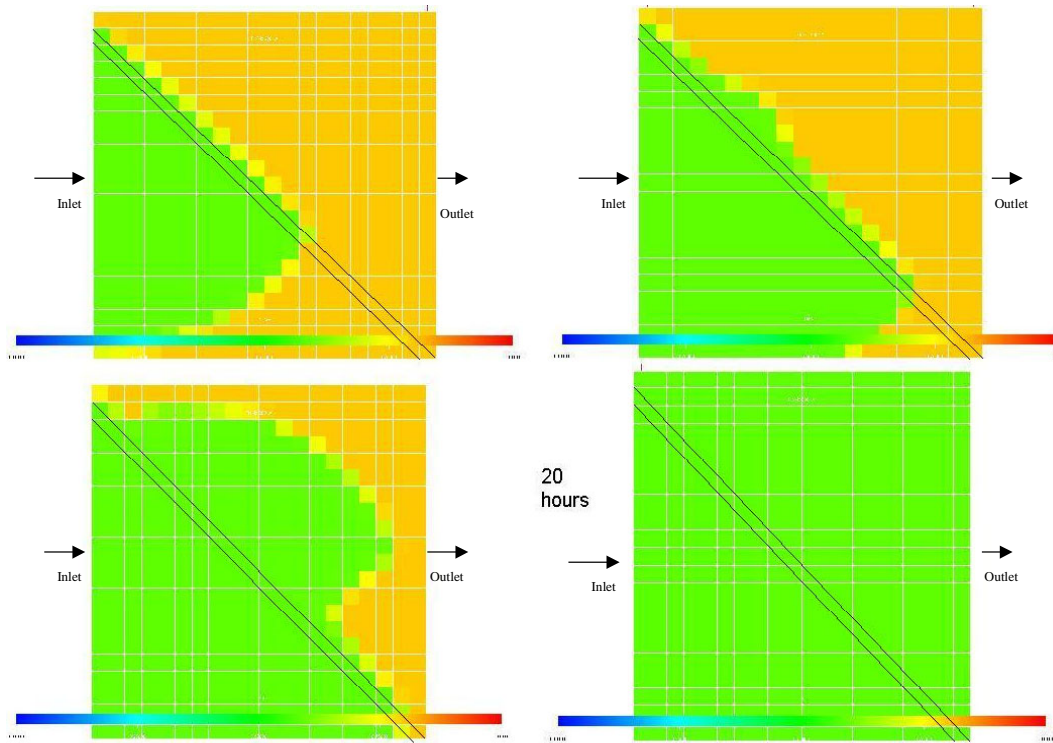
Figure 3.21: Saturation map for imbibition with inclined fracture connecting left and right faces of the core model. Fracture is located between the black lines.

Relative Permeability at Endpoint Saturations

The first set of endpoint saturation relative permeability experiments is labeled Experiment 1 and the next set Experiment 2.

The approximate steady state was taken to be at an inlet pressure of 300 psig. The pressure fluctuations are erratic and difficult to explain. The conceptual model developed and applied to the water absolute permeability experiment results is inadequate. The pressure spikes in Figure 3.22 can be attributed to interference between nitrogen and water flows in addition to the fracture behavior described in the conceptual model.

Steady-state for the gas injection of Experiment 1 was reached at a pressure of 78 psig and a flowrate of 0.16 L/min. The inlet pressure and flowrate data are shown in Figure 3.23.
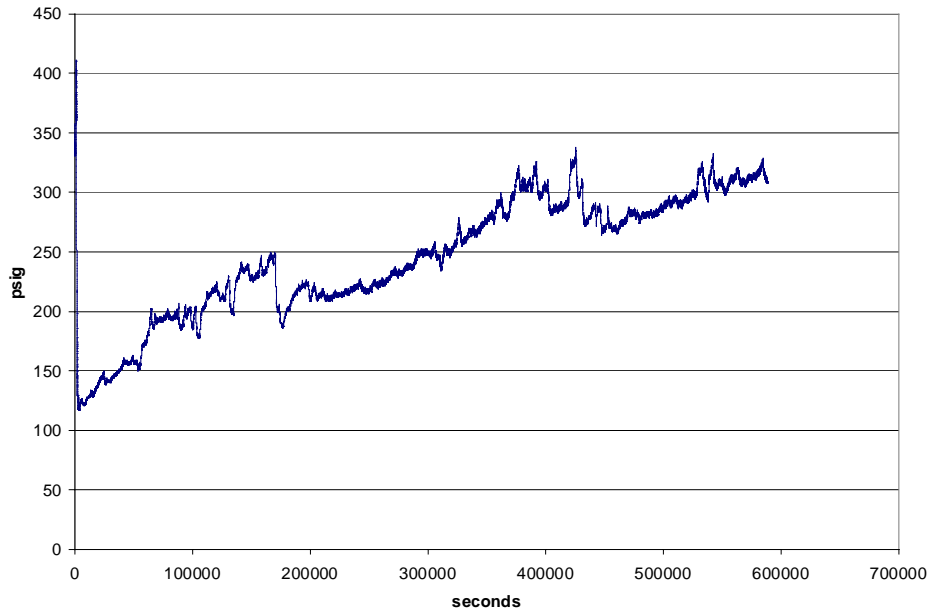
63

Figure 3.22: Pressure at inlet during water injection at constant water flowrate of 0.05 ml/min. From Experiment 1.
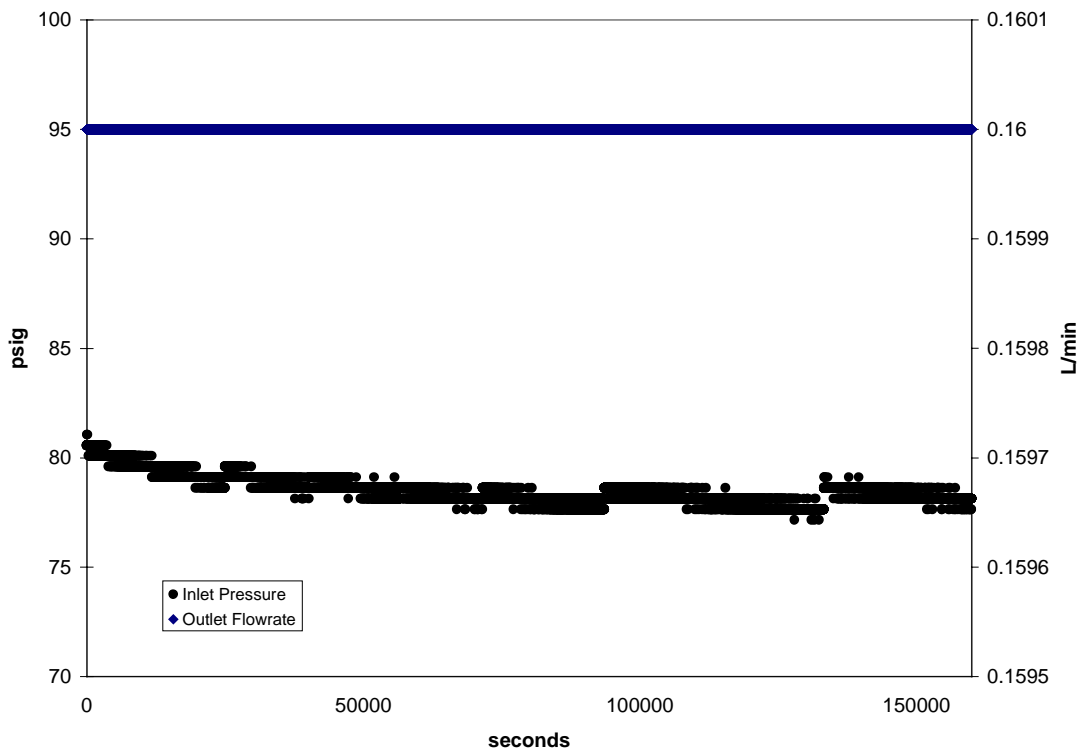

Figure 3.23: Pressure and flowrate at inlet during gas injection. From Experiment 1.

Experiment 2 results at irreducible gas saturation are presented in Figure 3.24. Steady state was at an inlet pressure of 580 psig. The sudden pressure drop of 350 psi at around 48000 seconds did not affect the cumulative water readings at the outlet and no changes were observed with the water pump. There was no gas seen with the deaerated water being fed to the pump. Such a huge pressure change can be caused by the formation of new flow pathways. This hypothesis is supported by the fact that steady state was realized at a pressure lower than 650 psig, where the pressure started to decline. The pathways may not have been accessible initially because of trapped nitrogen or closed fractures. However, in Experiment 1 where it is logical to assume similar events to occur the pressure drops observed were around 50 psi and did not occur as rapidly as the 350 psi drop in Experiment 2. It is therefore likely that the pressure drop in Experiment 2 was caused by fracture propagation. For materials with flaws, stress concentration will be high and fracture propagation/initiation occur well below the material's tensile strength.

Experiment 2 results at irreducible water saturation are shown in Figure 3.25. Steady state was at 83 psig and 60 ml/min.

The relative permeabilities using the different calculated absolute permeabilities and slip factors are listed in Tables 3.5 through 3.8.
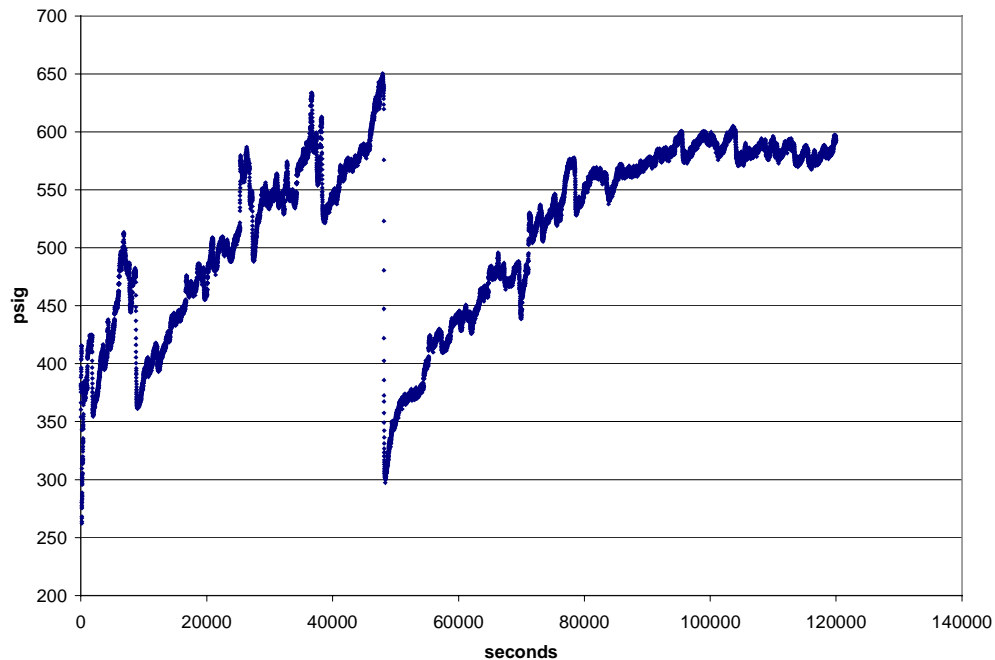

Figure 3.24: Pressure at inlet during water injection at constant water flowrate of 0.5 ml/min. From Experiment 2.
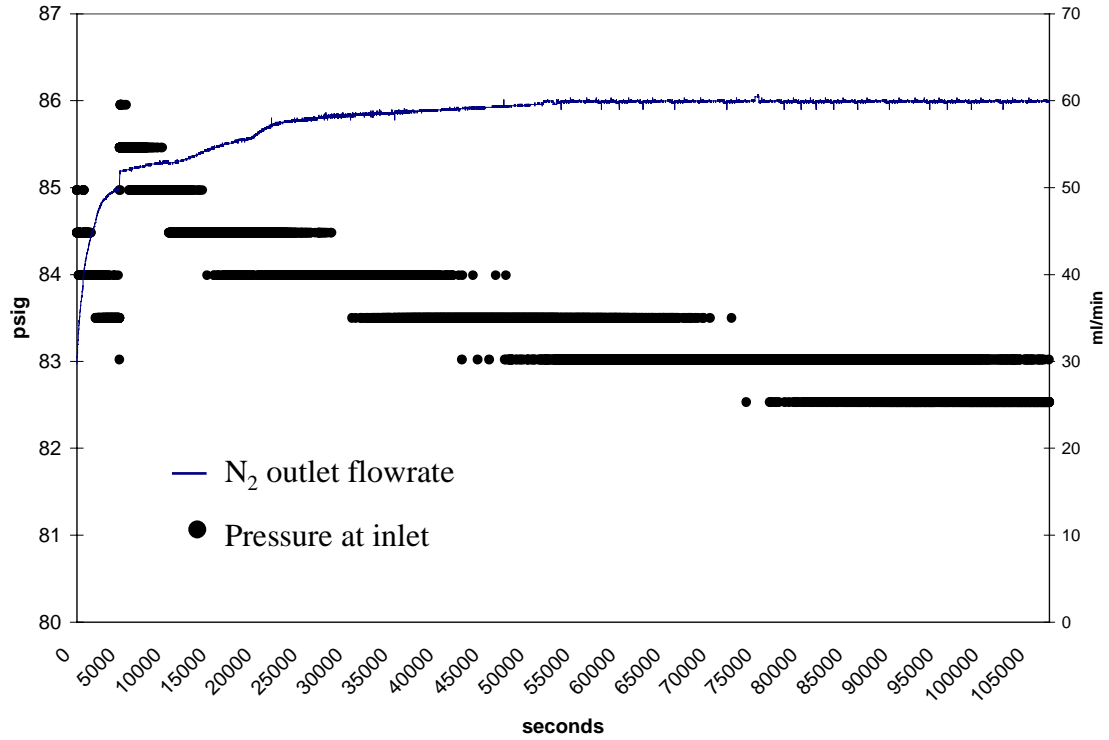
Figure 3.25: Pressure and flowrate at inlet during gas injection. From Experiment 2.

Table 3.5: Nitrogen gas relative permeability from Experiment 1.

k_{rg}	k_{abs}	b	Remarks
0.957	0.6	9.091	k_{abs} and b from N_2 gas experiment H
0.711	0.808	9.091	k_{abs} from water injection experiment @ 10 ml/min b from N_2 gas experiment H

Table 3.6: Nitrogen gas relative permeability from Experiment 2.

k_{rg}	k_{abs}	b	Remarks
0.709	0.35	7.143	k_{abs} and b from N_2 gas experiment L
0.238	1.0445	7.143	k_{abs} from water injection experiment @ 14 ml/min b from N_2 gas experiment L

Table 3.7: Water relative permeability from Experiment 1.

k_{rw}	k_{abs} (md)	k_{abs} obtained from
0.0134	0.6	N_2 gas experiment H
0.0099	0.808	Water injection experiment @ 10 ml/min

66

Table 3.8: Water relative permeability from Experiment 2.

k_{rw}	k_{abs} (md)	k_{abs} obtained from
0.1348	0.35	N_2 gas experiment L
0.0452	1.0445	Water injection experiment @ 14 ml/min

The absolute permeabilities from the water injection experiments at 0.1 ml/min and 2 ml/min are highly suspect because the water pump shut down during the 2 ml/min water injection experiment upon reaching the maximum pressure limit. The 0.1 ml/min water injection experiment followed the experiment at 2 ml/min. Air may have entered the core when the pump stopped. Thus, the relative permeability values obtained from the 0.1 ml/min and 2 ml/min experiments are erroneous.

Prior to the nitrogen experiment, L, the slip factor used was obtained from experiment H. Numerical simulations by Pruess and Tsang (1990) and Pyrak-Nolte et al. (1990) indicate significant phase interference resulting in the sum of relative permeabilities being less than 1. The sum of the relative permeabilities for Experiment 1 and Experiment 2 are all less than 1.
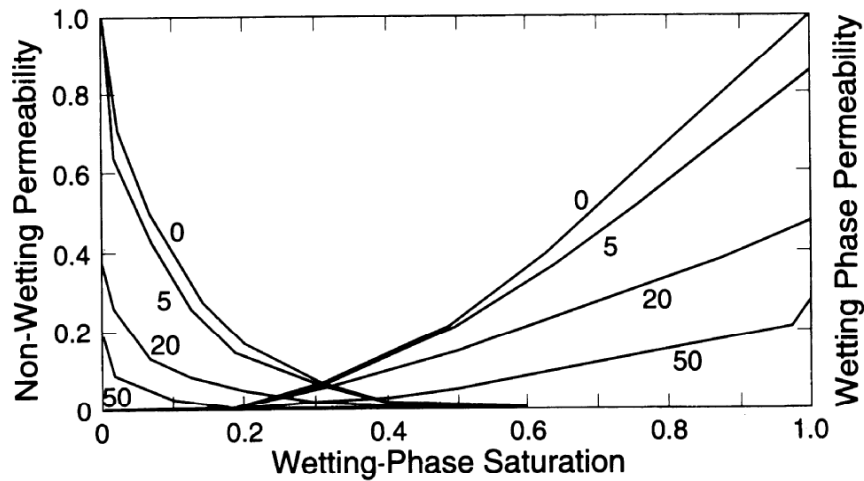

Figure 3.26: Simulation of effect of stress on relative permeabilities for a reduction in aperture of 5, 20, and 50 units of aperture. From Pyrak-Nolte et al. (1990).

The value of k_{rg} is much higher than k_{rw} at the endpoint saturations. The simulations by Pyrak-Nolte et al. (1990) show that this can occur at large apertures, as in Figure 3.26.

More insight may be gained by using the modified cubic flow equations for rough fractures by Cook et al. (1990). This equation is for single-phase flow only. Since the experiments were done at irreducible saturations then the equation may be applied for purposes of determining parameter effects and not for obtaining definite numerical answers.

$$q = \left(\frac{b^3}{12\mu}\right)\left(\frac{1-d}{1+d}\right)\frac{1}{f}\nabla p + q_\infty \qquad (3.15)$$

where b is a representative aperture

μ is the dynamic viscosity

d is the ratio of the contact area of asperities to the total fracture area

f is the friction factor

∇p is the pressure gradient

q_∞ is the irreducible flow, or the flow if there were no fractures

q is the actual flowrate

Equating this to $q = (kk_r A/\mu)\nabla p$ and solving for k_r,

$$k_r = \left(\frac{b^3}{12}\right)\left(\frac{1-d}{1+d}\right)\frac{1}{f}\frac{1}{kA} + \frac{q_\infty}{q} \qquad (3.16)$$

The ratio q_∞/q will be less than 1. Intuitively, this ratio will be lower for water than for nitrogen gas.

Also, assuming that b and d are the same for Experiment 1 and Experiment 2, then changes in the friction factor will determine the differences in relative permeability. The water flow will have lower Reynolds number and, consequently, higher friction factor than the gas flow. Thus, k_{rw} will be less than k_{rg} at irreducible saturations.

The wetting property of water may also have a decreasing effect on the friction factor of the gas flow. At irreducible water saturation, water will occupy the small spaces in the fracture surfaces and will reduce the surface roughness. A smoother surface will have a lower friction factor. The effect of the decrease in void volume, due to the presence of water within the fractures, may not be as significant as the reduction in surface roughness.

Nitrogen and Water Injection

Several nitrogen-water relative permeability experiments were conducted by injecting nitrogen and water into the core simultaneously. None of these experiments realized steady state.

The first few experiments were conducted at constant inlet flowrates for both water and nitrogen. Figure 3.27 shows the inlet pressure behavior of one of these experiments. The general pressure trend tends to stabilize at 60 psi. However, 100 psi pressure spikes are evident. This strange phenomenon may be explained by the fracture network conceptual model, which was applied to the absolute permeability water injection experiment. It can also be observed that the frequency of the pressure spikes increases with pressure. Looking closely at the pressure data of the water injection experiments at flowrates of 2 ml/min and 0.1 ml/min, Figure 3.14 and Figure 3.15, the magnitude of the pressure fluctuations and its frequency increase with inlet pressure. The lower net stresses at

higher inlet pressures causes the fracture apertures to be relatively more unstable. The changing phase structure, or the distribution of the phases in the fracture, further aggravates the instability.
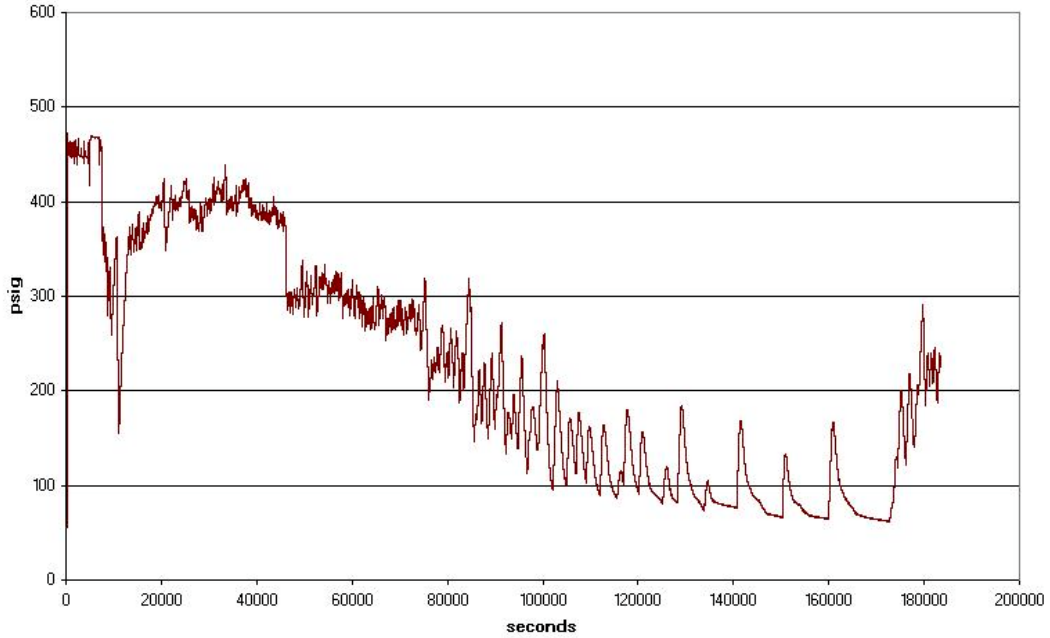

Figure 3.27: Pressure at inlet for constant flowrate nitrogen-water relative permeability experiment.
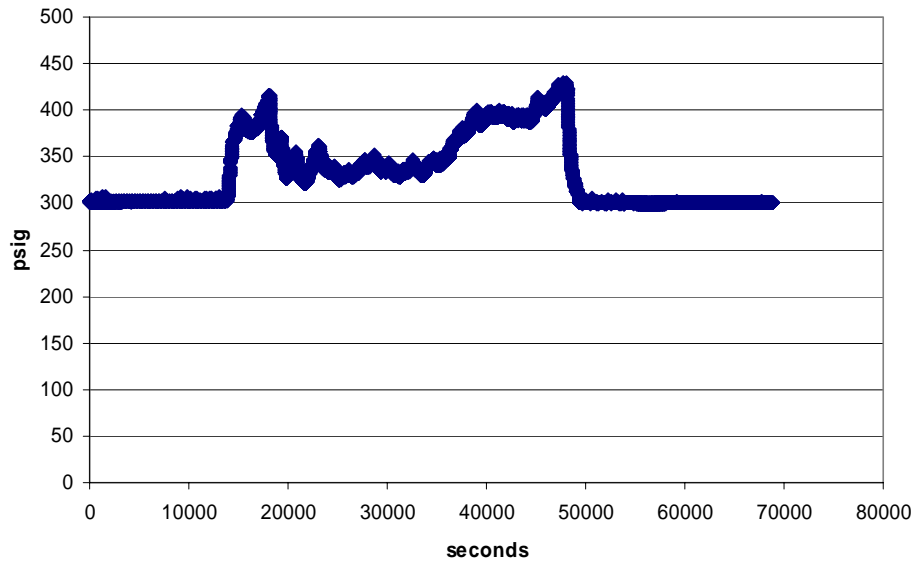

Figure 3.28: Pressure at inlet for nitrogen-water relative permeability experiment.
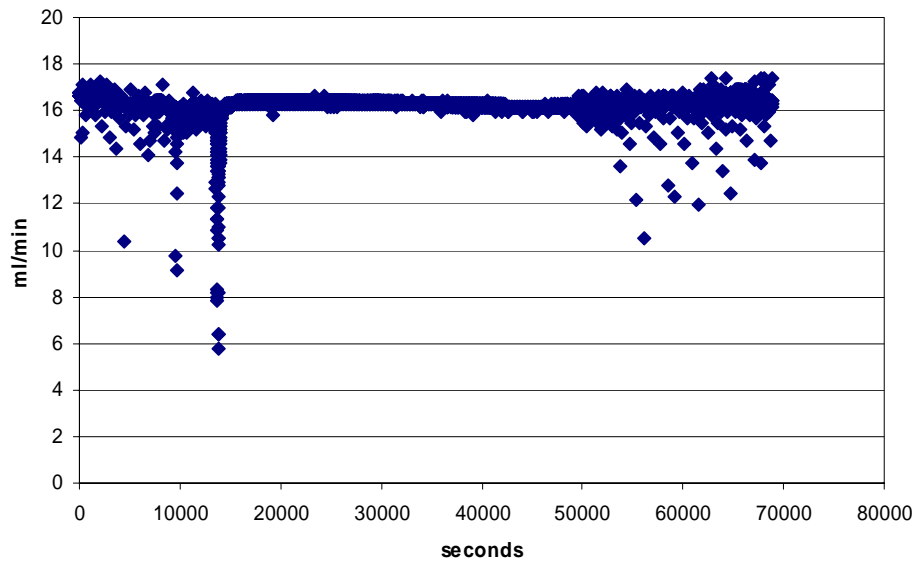
69

Figure 3.29: Nitrogen inlet flowrate for nitrogen-water relative permeability experiment.

The experiment shown in Figure 3.28 and Figure 3.29 was conducted at constant water flowrate. A pressure regulator controlled the nitrogen inlet pressure. Instability occurs in either the pressure or nitrogen flowrate. When the pressure is constant the nitrogen flowrate fluctuates and vice-versa. Phase interference may be the culprit.

3.4 CONCLUSIONS

The experiments conducted on The Geysers geothermal core were not all successful. However, data from this experimental study gives insights into behavior of fractures and fluid flow through these fractures that will be helpful in future research work. Basic geothermal rock properties such as irreducible saturations and porosity were determined.

1) The irreducible water saturation of The Geysers geothermal rock is approximately 15%. The irreducible gas saturation obtained is around 20%, but may actually be lower. Porosity of the core is 4.3%.

2) The resistivity method provides acceptable estimates of average water saturation in the core. The error is within ±5% compared to the values obtained by weighing the core.

3) At the endpoint saturations, the water relative permeabilities are much higher than the nitrogen gas relative permeabilities. This can be attributed to higher friction during water flows at irreducible gas saturation compared to nitrogen gas flows at irreducible water saturation. At irreducible water saturation, water will occupy small spaces in the fracture surface and reduce the surface roughness. Smoother surfaces have lower

friction factors. The decrease in void volume due to the presence of water within the fractures may not be as significant as the reduction in surface roughness.

4) Flow experiments in fractures are very much linked to the rock mechanics of the fractures. Fracture aperture, fracture roughness, and fracture propagation/initiation are affected by the number of loading cycles and the net stresses applied. Eliminating these changes to the core during an experiment will be the ideal case. Nonideal situations will require quantification of these changes and incorporating the changes into the flow calculations.

5) Further work is required to obtain relative permeability values for the whole saturation range. The steady-state experimental approach encounters difficulties due to phase interference and rock fracture changes. Steady state may be reached after an impractical length of time. The unsteady-state method should be pursued. In unsteady-state experiments the challenge will be in quantifying fluid flow changes in addition to rock fracture changes.

4. REFERENCES

Ambusso, W.J.: *Experimental Determination of Steam-Water Relative Permeability Relations*, MS report, Stanford University, Stanford, California (1996).

Amyx, J.W., Bass, D.M.Jr., Whiting, R.L., 1988, Petroleum Reservoir Engineering, Mc-Graw Hill, Inc..

Anderson E.M., 1951, Dynamics of Faulting and Dyke Formation with Application to Britain, Hafner Publishing Company.

Archie, G.E., 1950: "Introduction to Petrophysics of Reservoir Rocks," Bulletin of the American Association of Petroleum Geologists, vol. 34, no.5, p.943-960.

Bergosh, J.L., Lord, G.D., 1987: "New Developments in the Analysis of Cores From Naturally Fractured Reservoirs," SPE 16805.

Brooks, R.H. and Corey, A.T.: "Hydraulic Properties of Porous Media," Colorado State University, Hydro paper No.5 (1964).

Chen, C.-Y., Diomampo, G., Li, K. and Horne, R.N.: "Steam-Water Relative Permeability in Fractures," *Geothermal Resources Council Transactions,* Vol.26, 2002.

Corey, A.T., "The Interrelations Between Gas and Oil Relative Permeabilities," *Producers Monthly* Vol. 19 (1954), pp 38-41.

Diomampo, G., "Relative Permeability through Fracture", MS thesis, Stanford University, Stanford, California (2001).

Diomampo, G., Chen, C.-Y, Li, K. and Horne, R.N.: "Relative Permeability through Fractures," *Proc. 27th Workshop on Geothermal Reservoir Engineering*, Stanford University, Stanford, California, January 28-30, 2002.

Du, Y., Aydin, A., "Interaction of Multiple Cracks and Formation of Echelon Crack Arrays," International Journal for Numerical and Analytical Methods in Geomechanics, vol. 15, p. 205-218.

Fourar, M. and Bories, S.,: "Experimental Study of Air-Water Two-Phase Flow Through A Fracture (Narrow Channel)," *Int. J. Multiphase Flow* Vol. 21, No. 4, (1995) pp. 621-637.

Fourar, M., Bories., Lenormand, R., and Persoff, P.,: "Two-Phase Flow in Smooth and Rough Fractures: Measurement and Correlation by Porous-Medium and Pipe Flow Models," *Water Resources Research* Vol. 29 No. 11. November 1993, pp. 3699-3708.

Horne, R.H., Satik, C., Mahiya, G., Li, K., Ambusso, W., Tovar, R., Wang, C., and Nassori, H.: "Steam-Water Relative Permeability," *Proc. of the World Geothermal Congress* 2000, Kyushu-Tohoku, Japan, May 28-June 10, 2000.

Horne, R.N., Ramey, H.J. Jr., Shang, S., Correa, A., and Hornbrook, J.: "The Effects of Adsorption and Desorption on Production and Reinjection in Vapor-Dominated Geothermal fields," *Proc*. of the World Geothermal Congress 1995, Florence, Italy, May, 1995, 1973-1977.

Horne, R.N., Satik, C., Mahiya, G., Li, K., Ambusso, W., Tovar, R., Wang, C., and Nassori, H.: "Steam-Water Relative Permeability," presented at World Geothermal Congress, Japan, May 28-June 10, 2000.

Kneafsy, T. J. and Pruess, K.,: "Laboratory Experiments on Heat-Driven Two-Phase Flows in Natural and Artificial Rock Fractures," *Water Resources Research* Vol. 34, No. 12, December 1998, pp. 3349-3367.

Jolly, R.J.H., Wei, L., Pine, R.J., 2000: "Stress Sensitive Fracture-Flow Modelling in Fractured Reservoirs," SPE 59042.

Jones, S.C., Roszelle, W.O., 1978: "Graphical Techniques for Determining Relative Permeability From Displacement Experiments," SPE 6045.

Jones, F.O., 1974: "A Laboratory Study of the Effects of Confining Pressure on Fracture Flow and Storage Capacity in Carbonate Rocks," SPE 4569.

Leverett, M.C.: "Capillary Behavior in Porous Solids," *Trans*., AIME, **142**, 152-168, 1941.

Li, K., and Horne, R.N.: "Accurate Measurement of Steam Flow Properties," *GRC Trans.* **23** (1999).

Li, K. and Horne, R.N. (2001a): "An Experimental Method of Measuring Steam-Water and Air-Water Capillary Pressures," Proceedings of the Petroleum Society's Canadian International Petroleum Conference 2001, Calgary, Alberta, Canada, June 12 – 14, 2001.

Li, K. and Horne, R.N. (2001b): "An Experimental and Theoretical Study of Steam-Water Capillary Pressure," *SPEREE* (December 2001), p.477-482.

Lockhart, R. W. and Martinelli, R.C.,: "Proposed Correction of Data for Isothermal Two-Phase Component Flow in Pipes," *Chem. Eng. Prog.*, Vol. 45, No. 39, 1949.

Mahiya, G.F.: *Experimental Measurement of Steam-Water Relative Permeability*, MS report, Stanford University, Stanford, Calif., 1999.

Marder, M., Fineberg, J., "How Things Break", Physics Today (September 1996), American Institute of Physics.

National Research Council Committee on Fracture Characterization and Fluid Flow, Rock Fractures and Fluid Flow: Contemporary Understanding and Applications, National Academy Press, Washington D.C., 1996, p. 1-160.

Pan, X., Wong, R.C., and Maini, B.B.: Steady State Two-Phase Flow in a Smooth Parallel Fracture, presented at the 47th Annual Technical Meeting of the Petroleum Society in Calgary, Alberta, Canada, June 10-12, 1996.

Persoff, P. and Hulen, J.B.: "Hydrologic Characterization of Four Cores from the Geysers Coring Project," *Proc*. of 21st Workshop on Geothermal Reservoir Engineering, Stanford, Calif., 1996.

Persoff, P. K., Pruess, K., and Myer, L.: "Two-Phase Flow Visualization and Relative Permeability Measurement in Transparent Replicas of Rough-Walled Rock Fractures," *Proc. 16th Workshop on Geothermal Reservoir Engineering*, Stanford University, Stanford, California, January 23-25, 1991

Persoff, P., and Pruess, K.: "Two-Phase Flow Visualization and Relative Permeability Measurement in Natural Rough-Walled Rock Fractures," *Water Resources Research* Vol. 31, No. 5, May, 1995, pp. 1175-1186.

Pruess, K., and Tsang, Y. W.: "On Two-Phase Relative Permeability and Capillary Pressure of Rough-Walled Rock Fractures," *Water Resources Research* Vol. 26 No. 9, September 1990, pp 1915-1926.

Renshaw, C.E., Pollard, D.D., "An Experimentally Verified Criterion for Propagation Across Unbounded Frictional Interfaces in Brittle, Linear Elastic Materials," Int. J. Rock Mech., Min., Sci., & Geomech. Vol 32, no.3 p. 237-249.

Rose, W.D., 1948: "Permeability and Gas-Slippage Phenomena", 28th Annual Mtg. Topical Committee on Production Technology.

Sanchez, J.M. and Schechter, R.S.: "Comparison of Two-Phase Flow of Steam/Water through an Unconsolidated Permeable Medium," *SPE Reservoir Engineering*, Aug. (1990), pp 293-300.

Satik, C.: "A Measurement of Steam-Water Relative Permeability," *Proc.* of 23rd Workshop on Geothermal Reservoir Engineering, Stanford University, Stanford, CA (1998).

Scheidegger, A.E. *The Physics of Flow Through Porous Media*, 3rd ed., University of Toronto, Toronto. 1974.

Sinnokrot, A.A: *The Effect of Temperature on Oil-Water Capillary Pressure Curves of Limestones and Sandstones*, Ph.D. dissertation, Stanford University, Stanford, CA, USA (1969).

Sta. Maria, R.B. and Pingol, A.S.: "Simulating the Effects of Adsorption and Capillary Forces in Geothermal Reservoirs," *Proc*. of 21st Workshop on Geothermal Reservoir Engineering, Stanford, Calif., 1996.

Su, G. W., Geller, J. T., Pruess, K. and Wen, F.,: " Experimental Studies of Water Seepage and Intermittent Flow in Unsaturated, Rough-Walled Fractures*,*" *Water Resources Research*, Vol. 35, No. 4, April 1999, pp. 1019-1037.

Tsypkin, G.G. and Calore, C.: "Capillary Pressure Influence on Water Vaporization in Geothermal Reservoirs," *Proc*. of 24th Workshop on Geothermal Reservoir Engineering, Stanford, Calif., 1996.

Urmeneta, N.A., Fitzgerald, S., and Horne, R.N.: "The Role of Capillary Forces in the Natural State of Fractured Geothermal Reservoirs," *Proc*. of 23rd Workshop on Geothermal Reservoir Engineering, Stanford, Calif., 1998.

Witherspoon, P.A., Wang, J.S.W., Iwai, K. and Gale, J.E.: " Validity of Cubic Law for Fluid Flow in a Deformable Rock Fracture," *Water Resources Research*, Vol. 16, No. 6, 1980, pp 1016-1024.